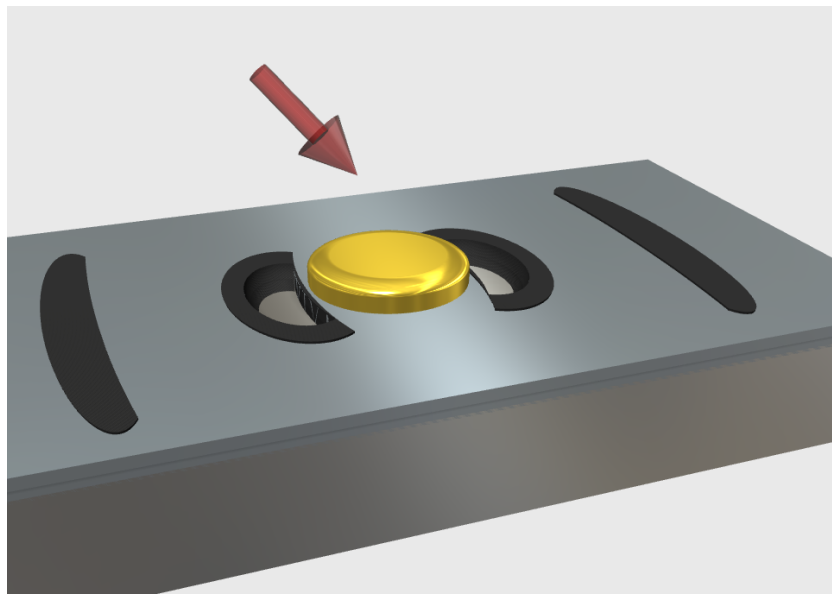


MAPPING OF  
NEAR-FIELD  
INTENSITY  
DISTRIBUTIONS  
BY ULTRASHORT LASER PULSES

-TOWARDS HIGH EFFICIENCY  
SOLAR CELLS



PETER L. TØNNING

Department of Physics and Astronomy  
Aarhus University



SUPERVISOR: PETER BALLING  
MASTER THESIS IN PHYSICS  
JULY 28TH 2016



## Abstract

This thesis presents an experimental platform for two dimensional mapping of the near-field induced by Localised Surface Plasmon (LSP) resonances. A theoretical introduction to plasmonic effects and how these result in field enhancement is presented along with theoretical background for the phase changing material GST. Experiments are conducted with a pulsed femtosecond laser system at tunable wavelength. The threshold fluence of GST for ablation and phase change is through experimental determination found to vary from 17.70 to 37.39  $mJ/cm^2$  over the spectral region of 1200 nm to 1570 nm. The mapping of the near-field is done by irradiating gold nano-discs placed on GST thin film. This results in short pulse excitation creating an imprint of the near-field by ablation and phase-shift from crystalline to amorphous bonding. The material alterations is subsequently detected on electron microscope. For single metallic disc the near-field is found to be in the shape of a dipole with additional field enhancement further from the particle present at wavelength around 1350 nm. The resonance of the dipole response is found to be at 1450 nm or higher. Experiments are further performed on pairs of nano-discs introducing coupling of LSP modes according to the plasmon hybridization model. The coupling leads to a red-shift of the LSP-resonance for light polarized along the axis of the pairs and a blue-shift for light polarized perpendicular to the axis of the pairs. This frequency shift is observed experimentally, however the resonance peaks lie beyond the spectral range of the irradiations and no quantitative measure of the frequency shift is found. Improved experimental mapping allows for reliable numerical simulations. The results in this thesis is thereby an important step towards full knowledge and control of LSP-resonances. This leads to applications for instance in relation to improving efficiency in solar-cells through spectral adjustment of the solar spectrum, which is the goal of the SunTune project at Aarhus University. Since this thesis is written as a sub-project to the SunTune project, the role of LSP's in improving the efficiency of solar cells is presented and discussed throughout the thesis.

---

# Contents

<b>1</b>	<b>Introduction</b>	<b>1</b>
1.1	Motivation . . . . .	1
1.2	Solar Cells . . . . .	2
1.3	SunTune . . . . .	6
1.4	Near-field mapping with phase-changing thin-film . . . . .	8
<b>2</b>	<b>Theory</b>	<b>10</b>
2.1	Plasmons . . . . .	10
2.2	Intensity enhancement by localized surface plasmons . . . . .	14
2.3	GST - a phase changing material . . . . .	22
<b>3</b>	<b>Ultra-fast lasers: Theory and experimental considerations</b>	<b>28</b>
3.1	Mode-locked femtosecond laser . . . . .	28
3.2	Tunable light source . . . . .	31
3.3	Optical setup . . . . .	35
<b>4</b>	<b>Experimental and characterization techniques</b>	<b>39</b>
4.1	LabView program . . . . .	39
4.2	Imaging techniques . . . . .	41
4.3	Sample preparation . . . . .	46
<b>5</b>	<b>Experimental work and data-analysis</b>	<b>50</b>
5.1	Short pulse excitation of GST . . . . .	50
5.2	Near-field patterns . . . . .	54
5.3	Quantitative near-field measurements . . . . .	58
<b>6</b>	<b>Results and discussion</b>	<b>62</b>

<i>CONTENTS</i>	iii
6.1 Near-field contour maps . . . . .	62
6.2 Coupled field enhancement . . . . .	67
<b>7 Outlook</b>	<b>73</b>
7.1 SunTune . . . . .	73
7.2 General usage . . . . .	74
<b>8 Conclusion</b>	<b>76</b>
<b>9 Dansk resume</b>	<b>78</b>
<b>Bibliography</b>	<b>81</b>

## Preface

This thesis serves to document almost a year of studying the near-field of nano-size metal-particles with possible use in future solar cells. My work in near-field mapping is a part of the SunTune project, a joint research project aiming to improve efficiency in solar-cells. This means that I have had the pleasure of working together with a large group of competent and helpful students, professors and technical staff. Additionally it means that besides my own work I have had the chance to participate in an academic environment with weekly discussions, collaborations between sub-projects and quarterly project meetings. I started on my master thesis just as the SunTune project started, and hence it has been a part of building up knowledge as well as experimental facilities in areas new to the department. As a consequence I have put an extra focus on experimental methods and characterization in this thesis as it has been my main contribution.

A special thanks goes to Søren H. Møller who has been my partner in most of the experimental work. I would also like to give my thanks to Peter Balling, who has been a knowledgeable and precise supervisor throughout the entire process. Finally thanks to my family who managed to proof-read parts of the thesis and Aske Krogsgaard who endured through the entire thesis providing valuable feedback. To the reader embarking on this thesis I have listed the chapters below along with a description of their content and function in the thesis as a whole.

**Chapter 1**, gives a mainly qualitative introduction to the work without going into technical details. This chapter also serves to include the solar-cell aspect of this project. A part of the work for my thesis has been the

participation in a 5 ECTS study group in the physics of solar cells. This is included as an extended motivation on the SunTune project and to maintain the wider perspective of my work.

**Chapter 2**, introduces the theory relevant to the work in this thesis. The chapter is based on a theoretical foundation of solid-state, molecular and optical physics and is quickly sharpened to the specialized theory necessary in this particular work.

**Chapter 3**, is a mixture of theory and documentation of the experimental procedures and -build regarding short pulse lasers. This part is included to reflect the fact that a great deal of the work on my thesis has gone into installing the brand new femtosecond laser system and subsequently building up the optical set-up for near-field mapping.

**Chapter 4**, describes the experimental methods used for fabricating and imaging the phase changing coating used. The chapter also includes documentation of the Labview implementation of the new laser-system with the experimental platform.

**Chapter 5**, presents the experimental results and method of analysis. Since the near-field mapping using Phase Changing Material (PCM) coating is an entirely new field of study at the department of physics in Aarhus the results will include both characterization of the PCM and demonstration of the near-field mapping technique.

**Chapter 6**, presents the measured near-field distributions. The near-field is characterized quantitatively on a nm scale and the results are discussed in relation to simulations as well as in relation to the Plasmon Hybridization Model.

**Chapter 7 and 8**, gives an outlook to the future development in the field as well as potential uses, naturally emphasising on solar cells. Finally the conclusion sums up the outcome of my work.

---

# Introduction

## 1.1 Motivation

There is no doubt that one of the modern society's greatest challenges is meeting the energy and electricity demands of our world without destroying the climate for future (and present) generations. The transition away from fossil fuels is governed mainly by mainly in the form of wind-, solar- or hydro-harvesting. The SunTune project aims to increase the efficiency of solar cells by expanding the spectral region accessible for electricity production. This is done by effectively converting the low-energy infrared light to light with photon energy suitable for solar cells. The method proposed for achieving this efficiency increase excels in the fact that it can be added on to already existing solar cells.

The details of the method will be explained in section (1.3). It should however already now be made clear that the SunTune project is a collaboration of many researchers and students and that my work is limited to the measurement of intensity enhancement by Localized Surface Plasmons (LSP's). This intensity enhancement can apart from the SunTune project be utilized in numerous application, all of which naturally also motivate the work in this particular thesis.

A key feature of LSP's is their ability to focus light down to feature sizes well below the diffraction limit, a fundamental optical barrier limiting the focus-size through conventional optics. Control over the focus shape and position at nm scale is a crucial step towards optical computing, securing future advance in computing power and data transfer speeds. The other main feature of the LSP's examined in this thesis is the intensity enhance-

ment. Tunable resonance frequency and intensity enhancement opens for applications in for instance nanoscale wavelength dependent light-detectors, as well as future cancer treatment[1].

Full utilization of LSP's requires a thorough understanding of the near-field of the plasmon resonance. Due to the small feature size, any measurement of the field distribution must circumvent the use of conventional optical microscopy because of the diffraction limit hindering resolution beyond  $\sim 200$  nm. Searching the literature one finds that there is no "standard" way of measuring the near-field of LSP's. This greatly hinders the advance of precise numerical simulation due to the lack of experimental comparison. The goal of this thesis is to produce an experimental platform for mapping the near-field of LSP's both spatially and spectrally. The procedure of this mapping will be qualitatively explained in section 1.4 while the theoretical background, experimental build and results constitute the remaining chapters of this thesis.

## 1.2 Solar Cells

Extracting energy from the sun is favourable due to a number of facts; the energy-flow in the sunlight is present all across the globe although in varying quantity. This along with the absence of moving parts and maintenance makes solar cell seem like a good choice, but does it really have the potential to cover the worlds energy demand? Measured inside the earth's atmosphere the energy current density (amount of sunlight) is,  $j_{E,AM1.5} = 1kWm^{-2}$ . When averaging out day and night and compensating for the angle of incidence at places off the polar axis the mean value is  $230 kWm^{-2}$ [2]. Taking Germany as example the available energy over a year is roughly  $3.6 \cdot 10^{14}kWha^{-1}$  whereas the energy demand of the country is approximately  $4 \cdot 10^{12}kWha^{-1}$ [2]. In other words, assuming 100 % efficiency of the solar cell, a coverage of  $\sim 1\%$  would cover the entire energy consumption of Germany. There are plenty of factors not taken into account in this number but it hints that solar power could indeed be a real contender on large scale energy supplies. An increase in solar cell efficiency would not only improve the large scale potential but also widen the use to devices where a high power pr area is crucial, eg. cars or mobile phones. Nonetheless there are a number of challenges along the way, and the efficiency becomes fundamentally limited well below 100 % as explained below.

## Semi-conductor based solar cells

A semi-conductor is a material with an electronic conductivity better than dielectrics but worse than metals. In terms of electronic properties this corresponds a filled valence band and an empty conduction band separated by a comparatively small band gap. Typically materials with band-gap energies up to a few electron volts are considered to be semi-conductors. The width of the band gap of semi-conductors compares in energy with the photon energy of the visible light spectrum, red light at 700 nm has a photon energy of 1.7 eV. Excitation of valence electrons in a semi-conductor is possible for all wavelength for which  $\hbar\omega \geq E_g$ , where  $\omega$  is the angular frequency of the incoming light and  $E_g$  the band gap energy. Due to the band structure, absorption in a semi-conductor produces, not only a free electron in the conducting band, but also a vacancy of charge (a hole) in the valence band. This duo of free charge carriers are the key to turning sunlight into electricity in a semi-conductor based solar cell.

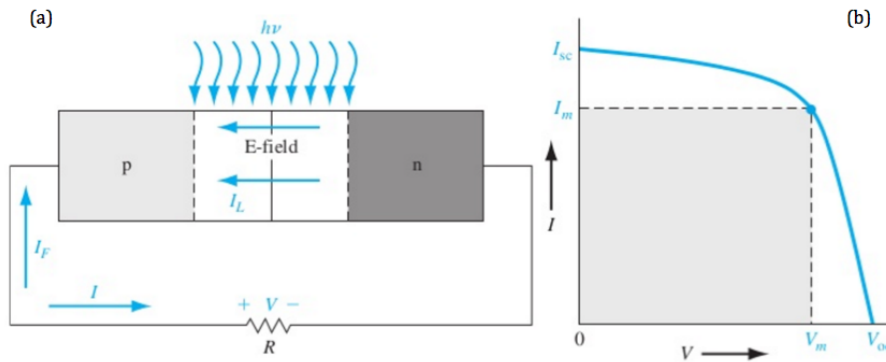


Figure 1.1: Shows the  $I/V$  characteristics of a  $pn$ -junction solar cell. (a) shows the connection of a  $p$ -type (light) semiconductor with an  $n$ -type (dark) creating a space-charge region between them resulting in an electric field. (b) Shows the  $I$ - $V$  curve of a solar cell. The area of the shaded square corresponds to the power extracted. Both figures are reprinted from [3].

Semi-conductors can be doped to have an excess of electrons ( $n$ -type) or an excess of holes ( $p$ -type), to various concentrations. Due to charge conservation the effect of this is to move the Fermi-level towards respectively the conduction band and the valence band. The solar cell is based upon the PN-junction where a  $p$ -type and an  $n$ -type semiconductor is joined together. In the vicinity of the junction electrons from the  $n$ -side will recombine with holes in the  $p$ -type, forming a region of positive and negative charge consti-

tuted by the ions. This *space charge region* produces an electrical field in the direction of the p-type as illustrated in figure 1.1a. Upon illumination and subsequent absorption in the space charge region the created electron-hole pair will be swept to each side by the E-field creating an electric current. The solar cell is rated in terms of power produced, given as the product of photo-current and voltage of the cell. The voltage has its maximum at  $V_{oc}$  where no current is flowing (hence  $R=\infty$ ) while the current cannot supersede the  $I_{sc}$  where the resistance falls to zero creating a short-circuit. The maximum power produced is found as a compromise between voltage and current as seen in figure 1.1b.

## Theoretical limit on solar cell efficiency

The ultimate goal of a solar cell is to convert as much of the energy current from the sun into electric energy. This conversion is limited on several fronts, some limits more fundamental than others. In order to illuminate the possibilities for efficiency improvement the most relevant limits will now be presented, going from the very fundamental towards limits specific to silicon PN-junction solar cells.

The most efficient engine imaginable is the Carnot heat engine. It is an academic exercise connecting a hot reservoir with a cold one, with a work being extracted via the heat flow. Taking the sun to be a black-body at 6000 K covering the solid angle  $\Omega_{emit}$  this constitutes the hot reservoir of a Carnot engine. Assuming that the sun is concentrated ideally upon a black body solar panel which absorbs light without increasing entropy, the efficiency is found to be[2],

$$\eta_L = 1 - \frac{T_{SP}^4}{T_S^4} - \frac{4T_0}{3T_S} \left( 1 - \frac{T_{SP}^3}{T_S^3} \right), \quad (1.1)$$

where  $\eta$  is the efficiency and the indices refer to Solar-Panel, Sun and  $T_0$  for an ambient temperature of 300 K. Equation 1.1 has a maximum of 96 % at low solar-panel temperatures and is called the Landsberg efficiency [2]. The Landsberg efficiency constitutes the absolute upper limit to any kind of solar conversion, however several assumptions such as ideal concentration, no increase in entropy and black-body absorption makes it merely a theoretical limit.

One aspect from the Landsberg efficiency that connects well with the semiconductor solar cells discussed above is the approximation of entropy free absorption. With photon energies matching perfectly with the band gap

energy the absorption process in a semi-conductor leads to no entropy increase. An aspect different from the blackbody absorption is that the efficiency of the semiconductor solar cell varies with photon energy. This can be explained from figure 1.1b. since macroscopic current corresponds to electron-hole current while voltage corresponds to the chemical potential of the electrons/holes. The IV-curve is thus different for different wavelengths of radiation and the maximum power is found at different currents. Considering a semi-conductor solar cells with layers tuned for band-gap energies all across the solar spectrum an upper limit for the efficiency of semi-conductor based solar cells can be determined. The efficiency for such an infinite-junction semi-conductor solar cell is found to be [4],

$$\eta_{SC} = \left(1 - \frac{T_{SP}}{T_0}\right) \left(1 - \frac{T_0^4}{f_\Omega \cdot T_S^4 + (1 - f_\Omega) T_{SP}^4}\right), \quad (1.2)$$

where  $f_\Omega$  is the incoming flux given by the solid angle of the sun. This results in a maximum efficiency of 86.8 % for concentrated solar light and 68.7 % for un-concentrated solar light.

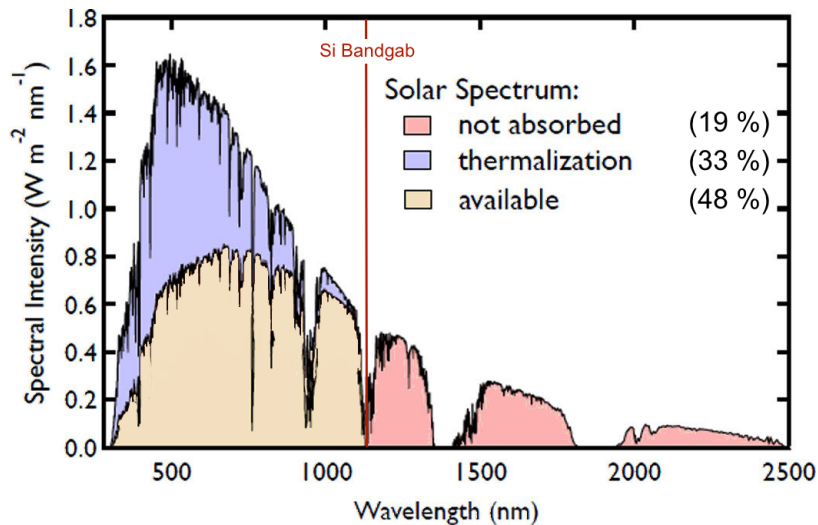


Figure 1.2: Shows the spectral intensity as a function of wavelength after absorption from the atmosphere. The red line indicates the smallest photon energy capable of exciting electrons across the silicon 1.1 eV bandgap, corresponding to a wavelength of 1130 nm. The figure has been recoloured and divided in to more suitable fractions for this thesis and is based on a spectrum taken from [5].

A multi-layer solar cell with infinite layers is still far from realistic though and a final angle to the maximum efficiency of a solar cell will be that of

a single layer silicon solar cell. Silicon has a band gap of 1.1 eV at 300 K, thus creating a cut-off in the absorption for all photons with an energy lower than 1.1 eV corresponding to a wavelength of 1130 nm. Further all photons with energies above the band gap energy will have part of their photon-energy contributing only to thermal relaxation in the silicon absorber. The combined effect of these losses is summarised in figure 1.2. The spectral losses (48 % available) combined with the limitations of a semi-conductor solar cell (68.7 % available) results in a final theoretical upper limit of 33 % for a single cell silicon cell[6]. This limit is known as the Shockley-Queisser limit and serves as an aiming point for the industry, where the record is at 25.6 % as of July 2015[7]. Over the last 20 years this number has seen no significant improvement, due to the immense challenge of reducing carrier recombination. In order to experience significant gains in performance it is necessary to circumvent the spectral and thermodynamic limitations by concentrating the sun-light, using multi-junction solar cells or by "adjusting" the spectral distribution of the sun. The SunTune project at Aarhus University aims to achieve the last of these by up- and down-converting photons with an energy less than the band-gap energy.

### 1.3 SunTune

The objective of the SunTune project is to present a method of utilizing a larger bandwidth of the solar spectrum in order to increase solar cell efficiency. To achieve this, researchers from the university departments of physics, nano-technology and engineering collaborate with solar-cell manufactures RAcel and energy provider EnergiMidt as well as the international partner ISC Konstanz. The SunTune project aims to up-convert photons with energy much lower than the band gap as well as down-shift photons with energy just below the band gap energy for subsequent up-conversion.

The down-shifting mechanism is based upon PbSe/PbS nano-crystals as previously reported in eg. [8]. The nano-crystals absorbs in the 1100 nm to 1480 nm range and re-emits at inside the Erbium absorption band. The up-conversion utilizes the Erbium ion ( $Er^{3+}$ ) which absorbs at 1480 nm to 1560 nm and re-emits at approximately 980 nm. Since the band gap energy of silicon corresponds to a photon wavelength of 1130 nm the Erbium ion effectively translates "useless" photons (including the down-shifted ones) into photons with very low thermal relaxation loss. This method opens for a potential efficiency increase of 4.7 percentage points, which is found by taking the distribution of photons and thermal losses from conversion

into account[9]. For the complete diagram of the energy flow see figure 1.3. Apart from the considerable increase in efficiency the introduction of up-conversion has some more indirect advantages. As already mentioned the match between Erbium irradiation and Silicon bandgap energy leads to less thermalization relatively and since efficiency scales inversely with temperature, higher efficiency on two accounts. Furthermore the access to infra-red photons greatly improves the efficiency under cloudy conditions and oblique angles (morning/evening) due to the reduced scattering of longer wavelength. This greatly improves the potential for solar cells in countries as Denmark and hints that the actual increase in energy output could very well exceed the relative increase expected from figure 1.3.

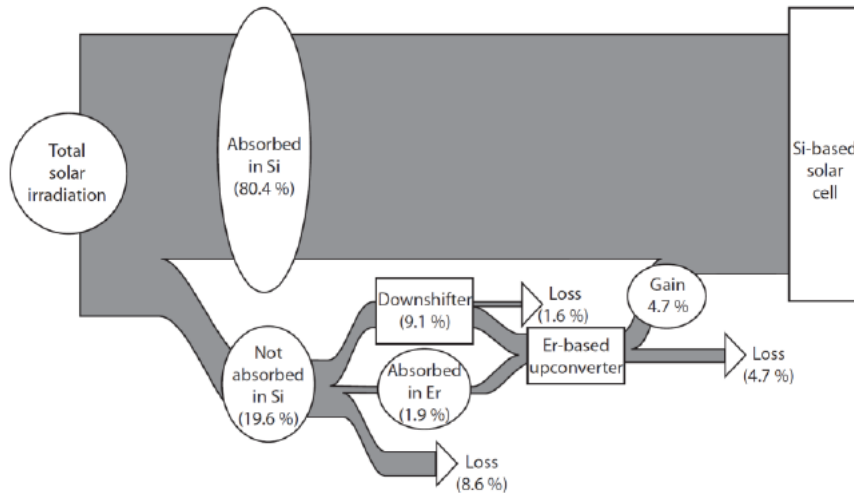


Figure 1.3: Shows the energy-flow for solar radiation utilized in a Si solar cell along with the potential for future increase. Note that from the 80.4 % absorbed in Si there is a loss of 33 percentage points to thermalization, this is not the case for the up-converted gain as this light is quite close to the band-gap energy and the thermal loss is minimal ( $\sim 10\%$ ). The figure has been reprinted from [9]

Especially the up-conversion process scales rapidly with intensity. This means that a "naked" Erbium based up-conversion layer will have very low conversion efficiency unless the solar light is somehow concentrated. The method pursued in the SunTune project is intensity enhancement by localized surface plasmons (LSP). Initial studies performed at Aarhus University shows an increase in conversion efficiency by more than 100 times by employing plasmons[10] (this study was for concentration of 808 nm light and

thereby not directly comparable to results in the SunTune project). The intensity enhancement is an effect of the near-field and is thus strongly dependent of the size and shape of the nano-particles supporting the plasmon resonances. In order to optimize the intensity enhancement, a part of the SunTune program serves to numerically simulate the LSP's as well as experimentally map the near-field of the nano-particles. The experimental mapping of the near-field is the part of the SunTune project pursued in this thesis and will be explained in greater detail in the following section.

## 1.4 Near-field mapping with phase-changing thin-film

Plasmons are in general defined by a resonance frequency and for LSP's also a characteristic near field distribution. This leads to measurements partly on large ensembles of LSP's giving only a smeared out extinction spectrum for the sum of nano particles of slightly different shape and size. Another approach is measurement of single particles. This for one returns the exact scattering spectrum for the chosen particle, but crucially single particle investigations can also give information of the near field distribution. The near-field of LSP's varies on a scale comparable to the size of the metal particle, in our case the nanometer regime. This makes depiction of the near-field a complicated task since there are no detectors available at this scale and optical methods of microscopy at this scale is fundamentally limited by diffraction. The imaging method first proposed for resolving the near field is scanning near field microscopy (SNOM or NSOM)[11]. SNOM relies on a probe (eg. optical fibre with nm aperture) that by scanning across the object translates the near field to an intensity distribution. This results in a resolution of  $\sim 50\text{nm}$ . Other methods for near field investigations has since been proposed, however, no clear preferred choice is found. The method pursued in this thesis is based upon using the near-field itself to alter the material on which the nano-particles are deposited. The alterations studied are primarily material ablation and change of molecular ordering. Common for the two alterations is that they require a certain threshold fluence to happen. Through precise control of the incoming laser fluence the goal is to map out the near-field by varying the incoming energy below threshold and subsequent detect areas with alterations as areas with respective field enhancement. Thus the method of this thesis has the potential to provide a quantitative measure of the near field at a resolution of  $\sim 10\text{nm}$ .

A feature of ultra-short laser pulses is the ability to expel material purely by achieving a sufficiently high energy density. This happens when the energy density of the laser-field becomes comparable to the binding energy of the material. In that way holes can be shot on the surface of basically any material for laser fluences above a material-specific threshold value. The ablation results in craters of increasing depth for increasing pulse energy, accompanied by a characteristic swelling along the edges[12]. The combination of steep edges and a rough crater makes ablated holes easy to detect with basically any imaging technique. The drawback of using ablation for near-field mapping is that the process is rather uncontrolled as cracks in the surface or dislocation in the crystal lattice can result in uneven holes.

The material alteration primarily investigated is the change from the crystalline to the amorphous state of the phase-change material GST. Phase Change Materials (PCM's) have long been used in rewritable optical media. The continuous switching between crystalline and amorphous bonding arrangements serves as the write/erase operation for GST-based optical media. This phase-change can be effectively performed by the use of ultra-short laser-pulses. Studies show that ultra-short (fs or ps scale) pulses can switch the GST from crystalline to amorphous state whereas longer pulses (ns scale) allows for crystallization, the reverse process[13]. The logic behind this is that the GST rapidly melts without evaporating, ultra-fast laser pulses does not supply heat long enough for the GST to recrystallize leaving it solidified amorphous. This is possible only within a certain laser-fluence threshold which corresponds to the crystallization temperature. The longer pulses allow for crystallization during the pulse whereas the short pulse destroys the inter-atomic ordering leaving the material melted for rapid cooling in an amorphous state. In order to read out the data written with the phase changes it is necessary to distinguish between the crystalline and amorphous state. The quantity used for this distinguishing is the reflectivity, which differs drastically in the two phases. Metal nanoparticles are placed on a thin-film of GST for experimental determination of the near-field from the LSP resonance. After irradiation from ultra-short pulses areas with intensity enhancement will appear as amorphous regions even well below threshold. Due to the diffraction limit the near-field pattern cannot be resolved simply by shining light and observing the reflection as with done with optical media. Instead the GST near the nano-particles are observed in a Scanning Electron Microscope (SEM) or an Atomic Force Microscope (AFM) giving nm resolution of the imprinted pattern.

---

# Theory

## 2.1 Plasmons

Plasmons are defined as plasma oscillations of free carriers, quantified in energy and thereby frequency. The excitation and propagation of plasmons can be studied for a number of geometrical viewpoints each with different characteristics. The localised surface plasmons which are central to this project are based on light interaction with metal. The interaction of light with metal will in this section be presented in an attempt to justify the use of nano-particles for efficient light manipulation.

In order to describe light-matter interaction of metals a suitable framework must be chosen. Maxwell's equations will be used in classical form, a good approximation for feature sizes larger than a few nanometer. Maxwell's equations will thus take the macroscopic form of

$$\nabla \cdot \mathbf{D} = \rho_{ext}, \quad (2.1a)$$

$$\nabla \cdot \mathbf{B} = 0, \quad (2.1b)$$

$$\nabla \times \mathbf{E} = -\frac{\partial \mathbf{B}}{\partial t}, \quad (2.1c)$$

$$\nabla \times \mathbf{H} = \mathbf{J}_{ext} + \frac{\partial \mathbf{D}}{\partial t}. \quad (2.1d)$$

Here  $\rho$  and  $J$  are the external charge and current while  $\mathbf{D}$ ,  $\mathbf{B}$ ,  $\mathbf{E}$  and  $\mathbf{H}$  denote the displacement field, magnetic field, electric field and the magnetizing field. For a linear, non-magnetic and isotropic media the material

response can then be reformulated as

$$\mathbf{D} = \varepsilon_0 \varepsilon \mathbf{E} = \varepsilon_0 \mathbf{E} + \mathbf{P}, \quad (2.2a)$$

$$\mathbf{B} = \mu_0 \mu \mathbf{H}, \quad (2.2b)$$

where  $\varepsilon_0$  is the vacuum permittivity and  $\mu$  the permeability constant, while the two unassigned  $\varepsilon$  and  $\mu$  are the material specific equivalent. With this formulation the dielectric function  $\varepsilon(\omega)$  becomes the key parameter describing electromagnetic radiation in a medium. From the dielectric function one can find the complex refractive index  $n$ , the complex conductivity  $\sigma$  and the extinction coefficient  $\kappa$ . Thus the dielectric function is a general measure of how a light field affects and is affected by a medium.

Metals are in the following described in the semi-classical Free-Electron model. This allows for details such as lattice potential, electron-electron interaction and band structure to be incorporated in the effective optical electron mass. The free-electron model describes the electrons of a metal as a uniform and negatively charged plasma surrounding fixed positively charged ions.

## Bulk plasmons

The coupling an electric field and the electron plasma results in a slight disturbance from the equilibrium state. The electron plasma is set into oscillation with respect to the ion background by an E-field with the ion-electron attraction constituting the restoring E-field. This motion can be described by harmonic equations on the form

$$m\ddot{\mathbf{x}} + m\gamma\dot{\mathbf{x}} = -e\mathbf{E} \quad (2.3)$$

Where  $m$  is the mass,  $\ddot{\mathbf{x}}$  and  $\dot{\mathbf{x}}$  the time derivatives of the displacement  $\mathbf{x}$  and  $\gamma$  the collision frequency of the electron plasma damping the motion of charge. The differential equation can be solved for the displacement which relates to the polarization as  $\mathbf{P} = -nex$ . From this the dielectric function is determined as[14],

$$\varepsilon(\omega) = 1 - \frac{\omega_p^2}{\omega + i\gamma\omega} \quad (2.4)$$

The frequency  $\omega_p$  is the plasma frequency of the metal given by[15]

$$\omega_p = \sqrt{\frac{n_e e^2}{m^* \varepsilon_0}} \quad (2.5)$$

Where  $n_e$  is the electron density,  $m^*$  the effective electron mass and  $\varepsilon_0$  the dielectric constant in free space. The electron-plasma oscillations are quantified in plasmons (or *bulk plasmons*, to distinguish from surface features), quasi particles of energy  $\hbar\omega_p$ .

The bulk plasmons is hence a longitudinal oscillation in the direction of propagation of the applied and restoring field. Light however has transverse polarization and thus cannot couple to bulk plasmons, in agreement with the initial observations on metals being highly reflective.

## Surface plasmon polaritons

Another type of plasmon is possible at the interface between a dielectric and a conductor (eg. a metal). The geometry of such an interface turns the dielectric function into effectively a function only of the spatial component perpendicular to the interface  $\varepsilon(\mathbf{r}) = \varepsilon(z)$ . Combined with equation 2.4 this leads to a wave equation on the form,

$$\frac{\partial^2 \mathbf{E}(z)}{\partial z^2} + (k_0^2 \varepsilon - \beta^2) \mathbf{E} = 0. \quad (2.6)$$

Here  $k_0$  is the wave vector and  $\beta$  the propagation constant of the travelling wave. Equation 2.6 is analysed in different interface geometries in various text-books, e.g. [14, 16]. The result is electromagnetic excitations propagating at the interface between a dielectric and a conductor, thereby confined in the plane of the interface. These oscillations are called Surface Plasmon Polaritons, or shorthand SPP's. Just like the bulk plasmon the SPP can be understood qualitatively from oscillating charges. If the charge density at the surface varies periodically along the interface, the field lines goes from the positive regions to the negative via both the conducting and dielectric side as seen in figure 2.1. This field geometry resembles that of a light wave propagating along the interface with polarisation perpendicular to the interface. For SPP's then it is indeed possible to make a coupling between light and surface plasmon, resulting in numerous application.

For this particular project the main interest about SPP's is the possibility to confine and hence enhance the electric field to volumes much smaller than the optical diffraction limit. This energy confinement can happen on scales well below the diffraction limit due to the short decay length into the metal [14].

For the SPP's there is still the challenge of coupling the light to the plasmon polariton. Direct illumination does not excite the surface plasmons as seen in figure 2.1 due to mismatch of the dispersion relations. Excitation can be

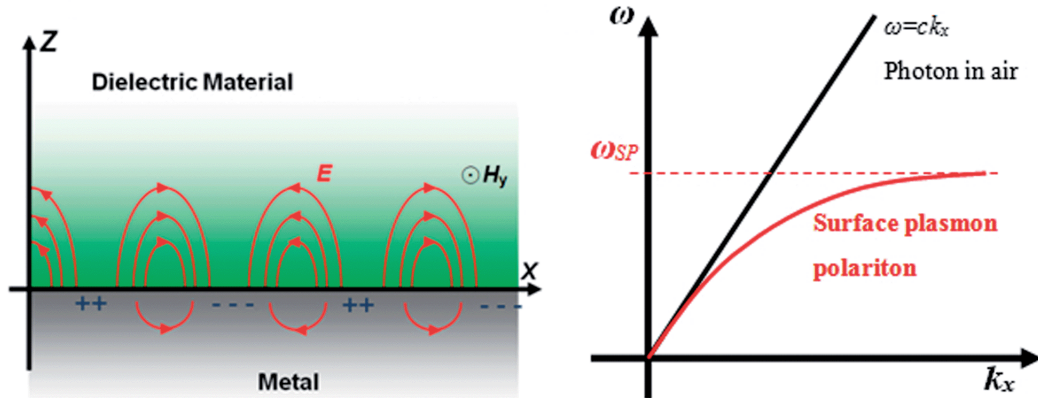


Figure 2.1: Shows the coupling of light with a surface boundary constituting a surface plasmon. To the right the dispersion relation shows how the plasmon couple to the specific frequency  $\omega_{SP}$ . Reprinted from [17]

achieved by the use of prism's or gratings or by creating symmetry on the scale of a wavelength.

## Localized surface plasmons

From the symmetry approach of SPP coupling inspiration is found for localized surface plasmons (LSP) where metal nano-structures facilitate the coupling with light. Localized surface plasmons are a result of a geometry outlined in figure 2.2. The plasmon response is induced in the same way as the bulk plasmon with the electron displacement producing the restoring force. For LSP's however the plasmon is pinned to the location of the metal nano-particle and is thus a non-propagating phenomenon. The oscillations occur with a resonance frequency determined by the charge density and thereby the geometry of the nano-particle. Noble metals have high electron density which lead to resonances in the visible and infra-red regime[11]. Due to damping in the metal, this phenomenon is not discrete in frequency but rather resonant over a frequency range determined by the losses in the metal.

Since the LSP responds to the field as an oscillation perpendicular to the direction of propagation it is possible to couple light directly to LSP's. At the plasmon resonance frequency this coupling is particularly strong and leads to considerable amplification of the E-field both inside the nano-particle and in its immediate vicinity, the near-field. From figure 2.2 an intuitive understanding of LSP resonances can be based on the oscillations

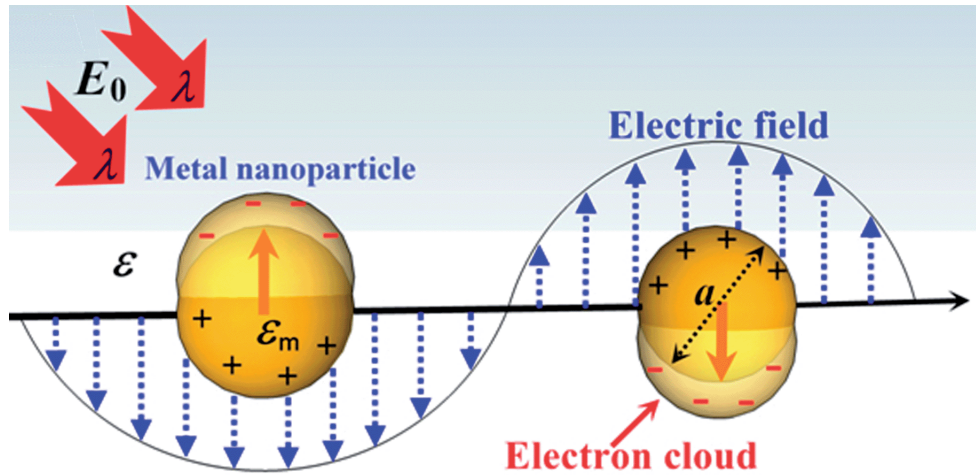


Figure 2.2: Shows the plasma oscillations of a nanosized metal sphere coupling to a light field. The E-field of the light is shown as blue arrows while the restoring field from the electron cloud is shown by a shaded red arrow. The shaded yellow sphere illustrates the displacement of the electron cloud. Reprinted from [17].

of the electron cloud. For wavelengths smaller than the nano-particle the resonance will correspond to multiple half waves along the particle surface. In the case where the nano-particle is smaller than the wavelength of the coupling field the electron oscillations becomes a collective motion for the entire nano-particle creating an oscillating dipole. The restoring force and thereby the resonance frequency of this dipole is highly depended on the shape of the nano-particle since electrons accumulate at the surface. This intuitive picture of the excitation of a LSP is in the following backed by the underlying theory and the resulting fields.

## 2.2 Intensity enhancement by localized surface plasmons

In order to describe the interaction of the metal nano-particles with light, the so called electrostatic approximation is made in the following. The logic of this approximation is that by assuming particle sizes well below the wavelength of light, the electric field can be treated as constant across each nano-particle. It is further assumed that the particle is spherical with diameter  $a$ , which yields symmetry around the azimuthal angle. This allows for an electric potential as the solution to Maxwell's equations expressed in

polar coordinates with  $\theta$  defined in relation to the electric field aligned along the Cartesian z-axis. The potential is expanded in Legendre polynomials as[14]

$$\Phi(r, \theta) = \sum_{l=0}^{\infty} (A_l r^l + B_l r^{-(l+1)}) P_l(\cos \theta), \quad (2.7)$$

where  $A_l$  and  $B_l$  are coefficients depending on the  $l$  quantum number while  $P_l$  are Legendre polynomials. The field is assumed to be parallel to the axis of symmetry, here taken as the z-axis. For large distances the potential should resemble that of the applied field only,  $-E_0 \cdot z = -E_0 \cdot r \cos(\theta)$ . Hence outside the particle  $A_1 = -E_0$  and  $A_{l \neq 1} = 0$  (as  $P_1(x) = x$ ). Inside the particle the potential must remain finite leading to the dismissal of the  $B_l$  terms due to divergence at  $r = 0$ . Finally equality of the tangential components of the electric field and normal components of the displacement field gives the form of the remaining two coefficients[14]. The final potentials inside and outside of the nano-particle are then given as:

$$\Phi_{out} = \left( \frac{\varepsilon - \varepsilon_m}{\varepsilon + 2\varepsilon_m} \cdot \frac{a^3}{r^3} - 1 \right) E_0 r \cos(\theta), \quad (2.8a)$$

$$\Phi_{in} = -\frac{3\varepsilon_m}{\varepsilon + 2\varepsilon_m} E_0 r \cos(\theta). \quad (2.8b)$$

Here  $\varepsilon$  and  $\varepsilon_m$  are the dielectric functions of respectively the nano-particle and the surrounding media, while  $\theta$  is defined as above in relation to the applied field. The potential outside of the particle is on the form of a dipole response to the applied field with the dipole polarizability of,

$$\alpha = \frac{(\varepsilon - \varepsilon_m)\varepsilon_m a^3}{\varepsilon + 2\varepsilon_m}. \quad (2.9)$$

Purely from the form of 2.9 it is clear that the field is resonantly enhanced at the condition  $\varepsilon = -2\varepsilon_m$ . As a matter of fact the possibility of higher order resonances also exist making the full requirement for resonance,

$$(l + 1)\varepsilon_m = -l\varepsilon \quad (2.10)$$

For a Drude metal at high frequencies ( $\omega\tau \gg 1$ ) this resonant condition can be expressed in terms of the angular frequency through the relation  $\varepsilon(\omega) = 1 - \frac{\omega_p^2}{\omega^2}$  (see e.g. [15]) giving,

$$\omega_l = \omega_p \sqrt{\frac{l}{l + (l + 1)\varepsilon_m}} \quad (2.11)$$

Taking the surrounding media to be air with  $\varepsilon_m = 1$  and looking only at the dipole excitation ( $l = 1$ ) the resonance is found to be,

$$\omega_1 = \frac{\omega_p}{\sqrt{3}} \quad (2.12)$$

Since the LSP's are treated in the electrostatic approximation the polarizability is directly coupled to the absorption and scattering cross-sections [18],

$$\sigma_{abs} = \frac{4\pi k}{\varepsilon_m} \text{Im}[\alpha] \quad (2.13a)$$

$$\sigma_{scat} = \frac{8\pi k^4}{3} |\alpha|^2 \quad (2.13b)$$

Inserting the polarizability from 2.9 the cross-sections for absorption and scattering are seen to scale as  $a^3$  and  $a^6$  respectively. This is intuitively understood by the fact that  $a^3$  is the volume of the nano-particle and naturally the absorption is dependent upon this, whereas scattering can be understood as absorption and re-emission and hence scales as volume squared.

The electric field is determined from eq. 2.8a and can be split up in the radiation field,  $kr \gg 1$ , and the near-field,  $kr \ll 1$ . The following field is found for the near particle regime,

$$\mathbf{E}_{nf} = \frac{3\hat{\mathbf{r}}(\hat{\mathbf{r}} \cdot \mathbf{p}) - \mathbf{p}}{4\pi\varepsilon_0\varepsilon_m r^3}. \quad (2.14)$$

Here  $\hat{\mathbf{r}}$  is the unit vector in the direction of the inspected point in space and  $\mathbf{p}$  is the dipole moment related to polarization by  $\mathbf{p} = \varepsilon_0\varepsilon_m E_0\alpha$ .

## Beyond single spherical nano-particles

It is clear from the cross-sections defined in 2.13b that the size of the particles constituting the LSP is crucial. Naturally the shape is of great importance as well. So far the derivations have all been based on spherical nano-particles, since this geometry allows for a fairly simple analytical solution. Going beyond the spherical geometry quickly makes everything much more complex. Results similar to those presented above can be found for ellipsoids as reported in eq. [14], [18] or [11]. Every structure beyond this, however, needs to be computed numerically. In figure 2.3 it is seen how the shape of the nano-particle shifts the resonance frequency. The study

in which figure 2.3 was presented clearly shows the importance of precise knowledge of the nano-particle as well as the need for experimental data to back simulations. The same paper further reports that geometric details such as the sharpness of the corners in a triangle influences the resonance frequency, albeit the shift in frequency is smaller than seen in figure 2.3

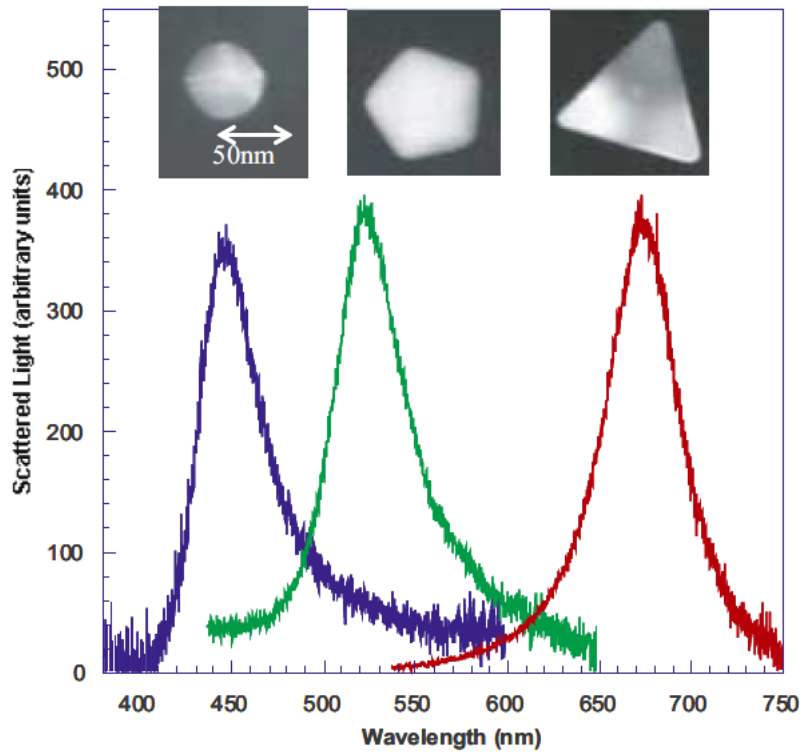


Figure 2.3: Shows optical spectroscopy measurements for three silver particles of similar size but different shape. The inserts show TEM images of the nano-particles responsible for each resonance. Reprinted from [19]

So far the focus has been on the light coupling of a single nano-particle. A lot of the potential in the field of LSP however lies in the coupling of multiple nano-particles for resonant plasmon phenomena. The coupling can happen via the far field as well as the near-field. Here the focus will be on the near-field coupling, meaning inter-particle distances comparable to or below the wavelength of the incoming light.

The near-field coupling between the LSP's can be understood by again considering the dipole field emerging from a spherical nano-particle. The effect of having more LSP's near each other can be analysed by considering the interaction of these dipoles. This approach to the coupling is called the *plasmon hybridisation model*, and excels in its ability to give an intuitive understanding to the shifts in resonance. With a dipole, the choice of orientation can be described as side by side (*sbs*) or end to end (*ete*), and then of course mixed cases for polarizations not aligned with the nano-particles. In figure 2.4 the possible configurations of two neighbouring dipoles can be seen. For the *sbs* configuration the force from the neighbouring LSP is counteracting the restoring force of the dipole oscillation. This corresponds to a rise in the resonance frequency. The same logic goes for the *ete* configuration where the dipole oscillation is enhanced, leading to a lower resonance frequency.

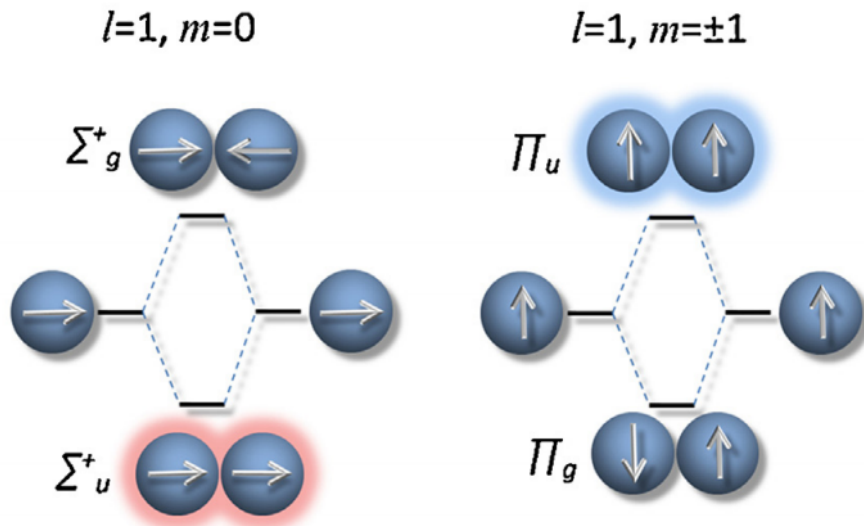


Figure 2.4: Shows the coupling of two adjacent LSP's. The dipole of the isolated particles can couple to a combined mode of either lower or higher energy. The panel to the left shows the *ete* configuration while the left panel shows the *sbs* case. Red and blue shadings indicate the bright modes and their shift in resonance frequency. This figure is reprinted from [20]

The full derivation of the energy shifts will not be presented here, but highlights are given in the following, based on chapter 4.1 in *Introduction*

to *Metal-Nanoparticle Plasmonics* by Pelton[11]. To examine the energy coupling present in these hybridization systems, the Lagrangian is a valid starting point. The continuity equation leads to a kinetic energy of,

$$T = \frac{1}{2} \int_S n_0 m_e \mathbf{v}^2 dV. \quad (2.15)$$

With  $n_0$  representing the electron number density. The potential energy is given by the charge shifted in the LSP. Assuming that the conduction electrons are incompressible, net charge can only be accumulated on the surfaces giving a potential energy of<sup>1</sup>,

$$U = \frac{1}{2} \int_S \int_S \frac{\sigma(\mathbf{r}_1)\sigma(\mathbf{r}_2)}{|\mathbf{r}_1 - \mathbf{r}_2|} dS_1 dS_2. \quad (2.16)$$

With  $\sigma$  representing the electronic densities at the point  $r$  in each particle. The Lagrangian, defined by  $L = U - T$  can then be used for calculating the dynamics of a combined system of more LSP's. The Euler-Lagrange equations for generalized coordinates  $q_i$  is given as,

$$\frac{d}{dt} \left( \frac{\partial L}{\partial \dot{q}_i} \right) = \frac{\partial L}{\partial q_i} \quad (2.17)$$

To advance from the Lagrange to the kinetics of the system a choice of geometry must be made. For spherical particles the solution is found to resemble the orbital solutions of atoms. Each coupling term is a Coulomb interaction between the corresponding spherical harmonics, giving combined solutions depending on quantum numbers  $l$  and  $m$ . Ignoring modes with  $l > 1$ , a frequency shift given by

$$\omega_{\pm}^2 = \omega^2 + \frac{|U_{1a1b}|}{2}. \quad (2.18)$$

Here  $U_{1a1b}$  is an interaction term on a form similar to 2.16, only with the electron densities expressed by spherical harmonics. The  $\omega_+$  solution corresponds to the situation with two dipoles out of phase, and as argued above the frequency increases. The  $\omega_-$  correspondingly represents a mode where the frequency is lowered. Apart from the changes in resonance frequency the dipole moment induced by the combined system determines the efficiency of the coupling with an incident plane wave (light). For the  $\Sigma$ -alignment (see figure 2.4) the  $\omega_-$  solution results in a combined dipole moment and

---

<sup>1</sup>Energy expression taken from [11, pp. 138] however in this reference a factor of  $\frac{1}{2}$  to account for double counting is wrongly omitted

thus an efficient coupling to plane waves. This orientation is referred to as a *bright* mode whereas the  $\omega_+$ -solution is a *dark* mode due to mutual cancellation between the two individual dipole moments. For the  $\Pi$ -alignment the  $\omega_+$ -solution is the bright mode and the  $\omega_-$ -solution the dark mode.

The hybridization model excels in its ability to calculate the LSP response of large arrays of simple particles as well as that of complicated particles by combining different simple particles. When the near-field coupling is strong, large dipoles develop across the gap between plasmonic particles, resulting in local fields much greater than the sum of the local field produced by isolated particles. On a side-note, the field from an array of coupled LSP's has two features that make the experimental mapping easier. Furthermore, the array has been found to be able to sustain itself even with smaller defects or missing Nano Particles (NP)[21].

With the introduction of mode-coupling the possibility of spectrally overlapping LSP-resonances arise. While LSP resonances and coupling of these are solely coulomb interactions, interference between the plasmon fields lead to a new response called Fano resonances. An illustrative example explaining Fano resonances is the overlap of a spectrally broad plasmon field  $E_b$  with a spectrally narrow plasmon field  $E_n$ . The fields are defined by a real and an imaginary part, describing respectively a dispersive response and an absorptive response. The real part thereby changes sign at  $\omega_0$  and is proportional to the width of the resonance while the imaginary part has a Lorentzian profile proportional to the field intensity. The total intensity will then be given as[11],

$$I_{tot} \propto |E_b + E_n|^2. \quad (2.19)$$

Equation 2.19 has a total of 4 contributions. The two initial resonances ( $I_b$  and  $I_n$ ), an interference between the two imaginary parts of  $E_b$  and  $E_n$  and finally an interference between the real parts of  $E_b$  and  $E_n$ . The imaginary interference  $I_{im}$  and the real interference  $I_{re}$  will only be non-zero at the overlap of the two initial resonances.  $I_{re}$  is then an asymptotic resonance at the narrow LSP resonance  $\omega_n$ .  $I_{im}$  is on the other hand a Lorentzian resonance with the width of the narrow LSP projected on the strength of the broad LSP at  $\omega_n$ . Fano resonances can thus be detected as narrow responses to the applied field, and depending on the dominating term in  $I_{tot}$  they will be either asymmetric or Lorentzian. This distinct response makes Fano resonances useful in determining individual LSP resonances.

## Modelling LSP response

Since the exact geometry of the nano-particle is so crucial to the light-coupling numerical simulations on specific particles are central in any full utilization of LSP's. Numerical modelling has not been a part of this project, however there is a strong collaboration with students within the SunTune project working on simulations. Work is being done both in simulating defined nano-structures as well as optimization towards the optimum nano-particle shape and pattern. In the following a qualitative overview of the simulation procedures is given.

The method used for calculating the near-field in the vicinity of nano-particles is known as the Finite Element Method (FEM). FEM is based upon dividing the domain in small (few nm's) elements of simple geometry (e.g. tetrahedrons). The total solution over the domain given by partial differential equation is thereby split into a number of discrete independent functions. Each of these functions are zero anywhere but within the belonging element, making the full solution a coupled set of linear equation. The electric field in relation to the magnetic field is defined in Faradays law of induction, see eq. 2.1c. Assuming no free charges and currents while taking the curl to this the expression becomes purely a description of the electric field,

$$\nabla \times (\nabla \times \mathbf{E}) = \nabla \times \left( -\frac{\partial \mathbf{B}}{\partial t} \right) = -\mu\epsilon \frac{\partial^2 \mathbf{E}}{\partial t^2} = \nabla^2 \mathbf{E}. \quad (2.20)$$

Here the two middle terms are found by substituting Amperes law in (eq. 2.1d), while the term to the right is a reformulation of the double-curl operation while assuming no free charge. The last two terms are on the form of an ordinary differential equation and is solved for each element.

The outcome is a solution to Maxwell's equations across the entire computational domain at a resolution determined by the element size and shape. The domain is constructed as a block containing layers of air, GST and silicon, with the gold particle placed in the middle, on top of the GST layer on the air side. The optical properties of air, gold and silicon are well tabulated whereas the properties for GST is measured. Since the solution is made in a 3 dimensional domain the electric field strength can be found in any given point surrounding the NP. The simulations presented in this thesis are all performed in the Comsol Multiphysics software by Emil Eriksen, a SunTune PhD.

An ongoing challenge in the SunTune project is optimization of the nano-particles. This is done by topological optimization, a method used in both

research and industry to optimize a parameter while minimizing another. Topological optimization is based upon a objective functional that are minimized through essentially picking a value of 0 or 1 for all points in the computation space. In the case of optimizing NP coverage, 1 then corresponds to gold coverage of the domain and 0 corresponds to no gold. The functional should additionally be designed to not only incorporate results from the FEM simulations but also practical restrictions such as limits in production. By minimizing through iteration the optimum distribution and shape of nano-particles are found. This is still a working progress, but eventually there will be a need for experimental mapping of the LSP near-field of these optimised nano-particles.

## 2.3 GST - a phase changing material

In order to map out the near-field a means of measuring the local field intensity is naturally needed. In this project Phase-Changing Materials (PCM's) known from optical data storage is used to directly imprint the field distribution. The switching between the amorphous and crystalline phases as described earlier is used to produce a binary distinction. This can be realized for a number of materials typically made from various combinations metalloids (semimetals). PCM's has numerous uses in technologies such as optical media for rewritable CD's and DVD's and perhaps future applications in optically based solid memory [22]. The PCM  $Ge_2Sb_2Te_5$  commonly abbreviated GST is widely used in photonics due to its ability to switch rapidly between the crystalline and amorphous state. The distinction between the two phases can be made either from the difference in optical reflectivity or the difference in electrical conductivity. Due to the widespread use of GST it is well studied and documented, making it ideal for this project exploring an alternative use of PCM's.

The switching and distinction between the amorphous and crystalline phase is clearly central to the utilization of GST. In order to understand the workings of GST in this particular project, the characteristic difference between the two phases and the excitation mechanisms are presented below. It should however be made clear that although rapid GST switching is widely used in the industry no full explanation of the reaction pathway has been agreed upon in the scientific community. The explanation presented in this thesis seems to be gaining support with articles published within the year supporting it.

## Phase-characteristics of GST phases

Solids in crystalline form are described from their crystal structure, a standardized description of the atomic ordering. GST will under the right conditions solidify in the face centered cubic-structure or simply fcc (c-GST). The stoichiometry of  $Ge_2Sb_2Te_5$  naturally makes the depiction as well as description of the crystal structure more complicated than the textbook example of fcc-ordering. The structure is, as seen in figure 2.5, comprised of two sub-lattices, one with Tellurium atoms and one with Antimony, Germanium and vacancies giving all of the atoms a coordination number of 6, vacancies included. For the amorphous GST (a-GST) the atoms are by definition with no ordering, in figure 2.5 the cubic representation of a-GST is however retained for easier comparison. In the amorphous state the coordination number is found to be the natural valence of each atom, meaning 2, 3 and 4 for Te, Sb and Ge respectively[23]. The twofold bonding of Tellurium leaves two 5p electrons constituting a lone pair, which has a key role in the properties of a-GST. The lone pairs further induce a number of defect states of either positively charged three fold coordinated atoms or negatively charged one-fold coordinated. The amorphous state thus becomes a mixture of Te chains and Sb planes held together by Ge.

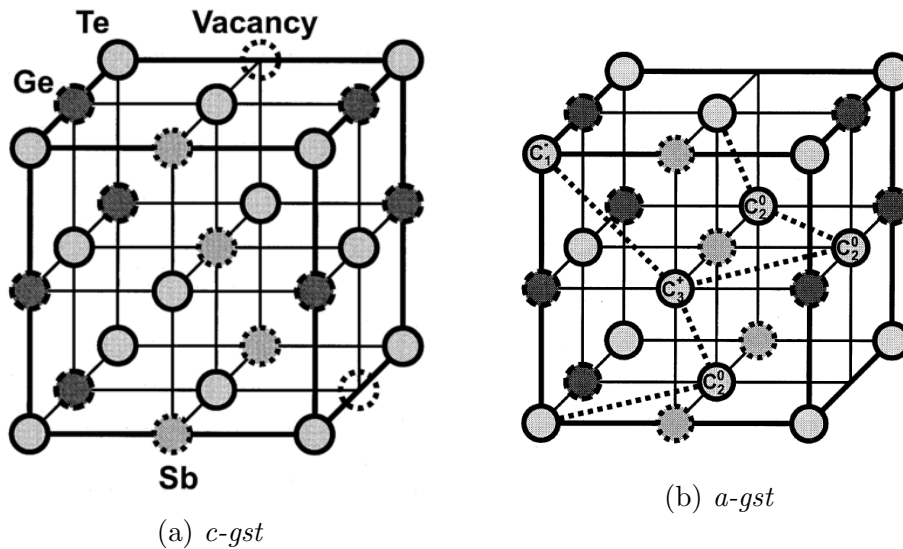


Figure 2.5: Shows the bonding and crystalline formation in GST. (a) show the fcc ordered crystalline structure with all atoms achieving 6-fold coordination, vacancies included. (b) shows the amorphous phase with the individual atoms binding according to the octant rule. Note that the ordering in (b) is artificial and only serves to ease comparison with (a). Reprinted from [23]

GST is in both of the two phases a semi-conductor with a band gap of 0.5 eV for c-GST and 0.7 eV for the a-GST[23]. The defect states of Tellurium creates trap states acting as both donor and acceptor levels in the amorphous phase. Since the photon energy of 1500 nm light is 0.83 eV this change in band gap should be considered as the nature of the excitation may change character towards a free carrier dominated excitation. More on this in the next section.

Apart from this  $\sim 20\%$  increase in band gap a much larger change in the dielectric function and thereby optical properties is reported [24]. In the range of 0.025 to 3 eV photon energy the dielectric function is 70-300 % larger for the crystalline GST configuration. Comparing the optical properties of GST with similar covalent semiconductor materials hints that the abnormality is in the crystalline phase. Investigations indicate that the key to this difference is in *resonant bonds*[24, 25, 26, 27]. In the crystalline phase ordering and alignment occur of p orbitals on adjacent molecular units, an effect is called resonant bonding. This alignment is lost in the amorphous phase where the p-orbitals form the dangling bonds. The impact of this change is a drastic increase in the optical matrix elements for the crystalline phase [27]. Thereby the change in optical properties is attributed to medium range ordering and not lattice deformations, which allows the switching process to proceed at a much shorter time-scale. This for one, allows for switching with ultrashort laser pulse, as is the case in this project, but similarly promises a possibility of high writing speeds in future data-memory applications. Relative changes in reflectivity of  $> 20\%$  has been achieved when switching from crystalline to amorphous GST with ultra-fast laser pulses [13].

## Excitation of GST by ultra-short pulses

Excitation of materials with femtosecond laser pulses requires a description with explicit timescales for electrons and ions respectively. The *two temperature model* was originally proposed in 1977[28], has been valuable in laying the theoretical ground for short-pulse excitation. Initially the electron and lattice is in equilibrium, with the electrons populated below the Fermi energy in the valence band or lower bands. As the pulse hits the surface, electrons from the valence band is rapidly excited to the conduction band. A combination of variations in energy origin and subsequent excitation from the conduction band during the pulse leaves the electrons in a non-equilibrium distribution at highly elevated "temperature". Tem-

perature is not defined at this point since temperature is a macroscopic quantity defined from equilibrium conditions. Collisions, both electron-electron and lattice-electron happen immediately upon excitation, however the large mass difference means that the electrons thermalize much faster than the lattice. Thus after a few femtoseconds the electrons has locally achieved equilibrium at a temperature of several thousand Kelvin, while the lattice temperature has hardly increased. At a picosecond timescale the electrons will eventually couple to the lattice leaving the combined material at a new equilibrium temperature well below the temporary electron temperature. Depending on this final temperature melting or ablation of the material can occur. The time evolution of electron and lattice in the two temperature model can be described by two coupled heat equations. Assuming a penetration depth much shorter than the size of focus, and that heat transport from the lattice to the electrons are negligible the system is described by[12],

$$C_e \frac{\partial T_e}{\partial t} = \frac{\partial}{\partial z} \left( \kappa_e \frac{\partial T_e}{\partial z} \right) - \Gamma (T_e - T_l) + Q(z, t), \quad (2.21)$$

$$C_l \frac{\partial T_l}{\partial t} = \Gamma (T_e - T_l). \quad (2.22)$$

Here  $C_i$  represent heat capacities,  $\kappa_i$  the heat conductivities,  $\Gamma$  the electron-lattice coupling and  $Q$  the power per unit volume absorbed from the laser. This seemingly simple relation of temperatures is greatly complicated by the fact that all quantities to varying extend depend on temperature.

Further complications arise from the fact that the two temperature model is primarily developed for metals and modifications must be considered when applying it to semi-conductors. Since the band gap of GST is 0.5 eV initial excitation with 0.83 eV (1500 nm) photons is possible only for the 0.33 outermost electrons energy-wise. The strong field present during the pulse does however allow strong-field ionization via multi-photon absorption or tunnelling ionisation[29, 12, 30]. Furthermore there will be a contribution to the excitation from free carriers already excited to the conduction band. The increasing amount of excited electrons increase the probability of impact ionization and Auger recombination. The outcome of these considerations are an electron-density-dependent two temperature model which allows studies of semiconductors in the same framework as metals[30]. A detailed description of the excitation of GST with 1500 nm fs-pulses is evidently complicated and beyond the scope this project. Keeping in mind that the excitation might be non-linear to some degree and

wavelength dependent the focus will instead be on the material alterations.

Laser ablation by ultra-short pulses is a threshold determined exclusion of material due to rapid heating, melting and evaporation. The ultra-fast time-scale of this process means that heat transport can be neglected resulting in a high localization of the ablation. Ablation is often defined by a threshold enthalpy change  $\Delta H$ , and in the framework of the two temperature model ablation occurs once the combined thermal energy of the electrons and the lattice exceeds this value[12]. This is formulated as,

$$C_l T_{l,max} + \int_{T_0}^{T_{max}} T_{max} C_e(T') dT' \geq \Delta H, \quad (2.23)$$

where the  $C$ 's is the heat capacity of the electrons and lattice while temperatures  $T$  are given as the lattice temperature after thermalization and the electron temperature distribution. The phase-switching of GST requires a slightly different description, as it cannot fully be described by the same threshold description. This is due to the changes in the reflectivity on electronic timescales that has been reported by e.g. [31] and [32]. The temporal description of the excitation of GST has recently resulted in a number of articles describing the ultra-fast switching capabilities of GST[25, 33]. The principle is outlined in figure 2.6 and is closely related to the two-temperature model.

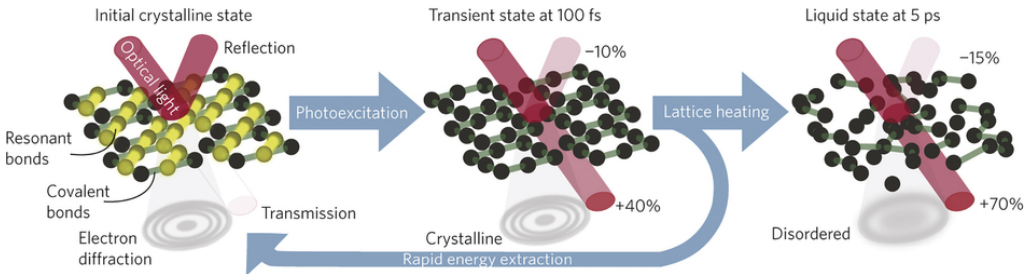


Figure 2.6: Shows the fast switching from crystalline to amorphous GST. The resonant bonds marked with yellow in the crystalline phase is dictating the optical properties allowing a rapid change in reflectivity upon rupture. The GST solidifies in the amorphous state preventing realignment of the resonant bonds. This figure is reprinted from [25]

A transient state is created within just 100 fs since resonant bonds are ruptured at electronic timescale. The optical reflectivity of the exposed GST area is thereby greatly lowered much faster than the melting and structural rearrangement can occur. This has great promises for improving the

switching frequency, at least one way, for data-storage utilization, however, for the use in this project a permanent change is needed.

The crystallization time of GST has been found to be approximately 500 ps, confirmed through both simulations and experiments [34, 35]. The electrons are superheated by the pulse and start colliding with the lattice reaching thermalization within 10 ps. By placing the thin film on a substrate with a high heat conductivity the heat is extracted before the crystallization can occur. The GST will therefore settle in the amorphous phase after thermalization, having a significantly lower optical reflection. The melting in addition leaves the material swollen due to a 6 % difference in density between the amorphous and crystalline phase [36], allowing for topological distinction between the phases by SEM or AFM.

---

## Ultra-fast lasers: Theory and experimental considerations

The change from crystalline to amorphous structure of the GST sample requires a short laser-pulse. In this particular project the laser-pulses are provided by a femtosecond laser system, named *Solstice Ace* from Spectra Physics. Since the laser system is based on a Ti-Sapphire oscillator the output has a central wavelength of 800 nm and hence must be converted to the desired wavelength range of 1480 to 1560 nm, matching the absorption range of the erbium up-converter. This conversion in wavelength is made utilizing the non-linear phenomena of white light generation and three wave mixing. The frequency conversion is performed completely automatic by the *TOPAS* and *NirUV* combination from Light Conversion. Finally the laser-beam of the desired frequency must be focused onto the sample and characterised in terms of energy, focus size and position. The three steps towards a laser pulse of suitable energy, temporal length and frequency are described in detail in the following subsections.

### 3.1 Mode-locked femtosecond laser

By nature a laser runs with continuous output at an equilibrium between the pumping to population inversion and the stimulated emission. Various techniques offer the possibility to modulate the lasing into pulse trains of intense laser-pulses. Many of these employ electronics for switching either the quality of the resonator or the pumping of the gain medium. For ultra-short pulses however one cannot rely on electronics since bandwidth and rise-time becomes limiting for sub nanosecond time-scales. To achieve sub

nanosecond pulses with ultra high peak power the method of mode-locking is instead used.

## Mode-locking

Mode-locking relies on the superposition of waves with different frequencies and by locking their modes together constructive interference at a single sharply defined time is created. A laser cavity constitutes a basis for a number of possible modes, standing waves, all fulfilling the boundary condition of nodes at the end-mirrors. For  $N$  different frequencies this results in a laser output in the form of a pulse train with pulse duration and peak intensity of,

$$\tau \approx \frac{T}{N} \approx \frac{1}{\Delta\nu_g}, \quad (3.1)$$

and

$$E_{peak} = \frac{NE_0}{2} \Rightarrow I_{peak} \propto |N \cdot E_0|^2. \quad (3.2)$$

Here  $E_0$  denotes the electric field amplitude of each mode (taken to be equal for simplicity) and  $\Delta\nu_g$  the spectral width of the gain-medium[37]. It is clear that a gain medium with positive gain for a broad range of frequencies is needed to narrow down the pulse width. Titanium sapphire is ideal with absorption from 450 to 600 nm and emission in frequencies between approximately 650 and 950 nm[38]. For a resonator in "lab scale" ( $\sim 1$  m) this corresponds to several hundred thousand lasing frequencies and a pulse-duration of less than 6 fs has been achieved purely from mode-locking of Ti:Sapphire lasers[39].

An effect that must be considered once working on a femtosecond time-scale is the Fourier Transform Limit. Since the pulses via Fourier transforming can be split in their spectral components there is a minimum value of the pulse-duration versus spectral width product. The minimum value depends on the spectral distribution of the pulse and is for a Gaussian spectral distribution found to be 0.44 using the FWHM as pulse-width in the time and frequency domain [40]. Assuming a spectral width of 300 nm centered at 800 nm the minimum pulse-duration is found to be,

$$\tau \geq \frac{0.44}{c \cdot \left( \frac{1}{650nm} - \frac{1}{950nm} \right)} \approx 3fs.$$

Not only does the Fourier Limit constitute a theoretical lower limit to the pulse duration, it also serves as a reminder of the uncertainty principle in

action. The fact that every ultra-short pulse is composed by a range of wavelength must be in the back of ones head constantly in the optical design of experiments.

In the Solstice Ace laser-system the oscillator (individually called the *MaiTai*) produces a pulse-train at 85 MHz rep rate and pulse duration of less than 20 fs<sup>1</sup>. The spectral width of the pulses are 60 nm corresponding to a fourier limited pulse duration of 15 fs. The temporal locking/matching of the modes is achieved by designing the cavity to favour pulsed operation. This is done by spatially overlapping the beam-waist of the  $TEM_{00}$ -mode with the pumped gain medium. To initiate the pulsed operation an acousto-optic modulator disturbs the system into mode-matching when the laser starts up[41]. Once "running" mode matched the higher Q-factor in the cavity for pulsed operation ensures that the mode-matching is maintained, mode-locking is thereby achieved.

## Chirped pulse amplification

The pulses coming directly from the oscillator are rather weak in pulse energy and thus needs to be amplified. Due to the short pulse-length the peak power is however rather high and simple amplification by a pumped gain-medium would lead to a number of non-linear effects distorting the focus or simply ablation of the optical equipment. To prevent this the method of chirped pulse amplification is used as sketched in figure 3.1.

By exploiting the spectral width of the pulse in a setup with two gradings, the frequency components are shifted in time creating a longer pulse. Due to different path-lengths the "red" part of the spectrum gets shifted temporally with respect to the "blue" part. With the grating spacing and spectral width of the Solstice system the 20 fs *MaiTai* pulse is stretched to a picosecond chirped pulse. Amplification can now be done using a pumped gain medium (Ti-Sapphire), where the pulse energy is increased by a factor of 3-4 for each passing. By picking out only a fraction of the pulses from the oscillator a big population inversion can be achieved and thereby a big increase in pulse energy. Each pulse picked out for amplification completes 10 or more runs through the gain medium, until the gain is saturated. The net amplification in energy of the Empower amplifier in the Solstice Ace is

---

<sup>1</sup>Information directly from Spectra Physics response to the requirement for the laser system when the system was chosen, no exact numbers are given in the official spec-sheet of the laser-system.

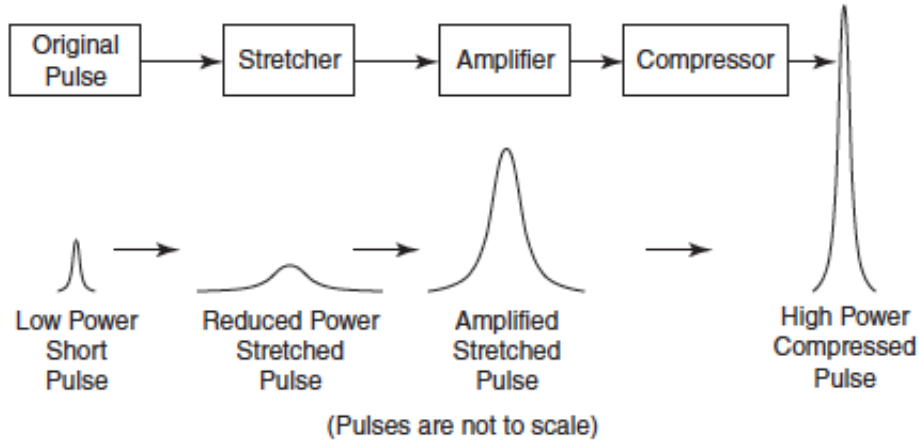


Figure 3.1: Shows the chirped pulse amplification scheme in steps. Note that the pulses are not to scale as the broad pulse in the amplifier is actually a factor of  $\sim 50$  times broader than the oscillator pulse. Similarly the amplitude of the pulses differ by several orders of magnitude. Reprinted from [42]

up to a factor of a million. After amplification the pulse is re-compressed down to a final pulse-length of 35 fs and pulse energy of up to 1.4 mJ.

## 3.2 Tunable light source

Since the Solstice system is based on a Ti-Sapphire gain medium the central wavelength is 800 nm. Absorption in the erbium ions happens at 1480 to 1560 nm and thus frequency conversion with ability to tune the wavelength is needed for studying the effects of plasmonics in erbium up-conversion. Fundamental to this conversion is non-linear light-matter effects as described below.

### Non-linear optics

Up until the advent of the laser in the 1960's light propagation through all materials was thought to be linear. Linear in propagation meaning no interaction of beams overlapping, no change in frequency and no dependence of intensity in material properties. From 50 years laser based experiments it is now well known that materials do in fact express non-linear interaction with light. The origin of the non linearities lies in the dipole interaction of the outer electrons with the light field. For small electron displacements the movement is proportional to the E-field, however just as is the

case with a classical spring increasing the amplitude makes the response increasingly an-harmonic. The non-linear response thus becomes significant when the light field (displacement force) becomes comparable with the inter-atomic E-field (elastic restoring force), typically at field intensities of  $\sim 10^{10}V/m$ [43].

Assuming that the non-linearities are small enough to be considered a perturbation the material response can be described as a Taylor expansion of the polarization density. Using the susceptibility  $\chi$  (related to the dielectric function by  $\varepsilon/\varepsilon_0 = 1 + \chi$ ) as measure of material response the polarization density becomes on the form[43],

$$\mathbf{P} = \varepsilon_0 (\chi^{(1)}\mathbf{E} + \chi^{(2)}\mathbf{E}^2 + \chi^{(3)}\mathbf{E}^3 + \dots). \quad (3.3)$$

Naturally eq. 3.3 alters the wave-equation and the resulting description of the light field. Examining the consequences of each term with an applied field leads to effects such as second harmonic generation and three wave mixing for the  $\chi^{(2)}$ -term, while for the  $\chi^{(3)}$ -term for instance white light generation and self focusing arise. For the purpose of frequency conversion the phenomena three wave mixing and white light generation is employed, however it should be noted that other non-linear effects must be considered once working with a high power laser beam. Since the Solstice output of 1.4 mJ pulse energy corresponds to a power of  $4 \cdot 10^{10}W$ , field intensities exceeding  $10^{10}V/m$  are obtained for any focus smaller than  $\phi 20\mu m$ .

Considering a field with two different spectral components  $\omega_1$  and  $\omega_2$ ,

$$\mathbf{E}(t) = \frac{1}{2} (E_1 e^{-i\omega_1 t} + E_2 e^{-i\omega_2 t} + c.c.) \quad (3.4)$$

This field is assumed to have intensity high enough to make the quadratic non-linear term of eq. 3.3 significant, but higher orders negligible. The non-linear polarization density will then have 5 components at 5 corresponding frequencies,

$$\mathbf{P}_{\chi^{(2)}} = \frac{\varepsilon_0 \chi^{(2)}}{4} \left[ (|E_1|^2 + |E_2|^2) e^0 + |E_1|^2 e^{i2\omega_1 t} + |E_2|^2 e^{i2\omega_2 t} + 2E_1 E_2 e^{i(\omega_1 + \omega_2)t} + 2E_1 E_2^* e^{i(\omega_1 - \omega_2)t} + c.c. \right]. \quad (3.5)$$

Each of these components corresponds to phenomena also known as Electro-Optical Rectification (EOR), two instances of Second Harmonic Generation

(SHG), Sum Frequency Generation (SFG) and Difference Frequency Generation (DFG) respectively. As a combined description the conversion processes for the second order non-linearity are called three wave mixing.

For the generation of a White Light Continuum (WLC) one has to look to higher orders of non-linearity. Considering now the interaction with a centro-symmetric material (such as sapphire), the even terms in equation 3.3 vanish leaving the cubic term as the dominant non-linearity. Since the refractive index is a function of  $\chi$  the refractive index gets a non-linear contribution, proportional to the field intensity:

$$n^2 = 1 + \chi^{(1)} + \frac{3}{4}\chi^{(3)}\mathbf{E}^2 \rightarrow n = n_0 + n_2I \quad (3.6)$$

The non-linear phenomena of three wave mixing and the intensity dependent refractive index is in the TOPAS/NirUV utilized for tuning the wavelength of pulsed laser-light.

## Frequency Conversion

Since the lasers inducing non-linear effects are pulsed the power at a certain point in the non-linear medium varies in time. Assuming a Gaussian temporal shape the intensity as a function of time is therefore given by,

$$I(t) = I_0 e^{-\frac{t^2}{\tau^2}} \quad (3.7)$$

Referring to equation 3.6 there must then be a time-varying refractive index producing a shift in phase and finally a shift in frequency. Propagation of a laser-pulse with central frequency  $\omega_0$  through a NL centro-symmetric media of length  $L$  results in,

$$\phi(t) = \omega_0 t - \frac{\omega_0}{c} n(I)L, \quad (3.8a)$$

$$\omega(t) = \frac{d\phi(t)}{dt} = \omega_0 + \frac{2\omega_0 n_2 I_0 L}{c\tau^2} \cdot t \cdot e^{-\frac{t^2}{\tau^2}} \quad (3.8b)$$

The spread in wavelength thus depends on both pulse-duration, NL-media, peak power, length of passage e.t.c. The effect is white light generation since the spectral output under right conditions spreads across the entire visible range. As an order of magnitude of the frequency spread it is seen in figure 3.2 that a 75 fs laser-pulse with a central wavelength of 800 nm

produces a White Light Continuum (WLC) from 450 to 1000 nm after passage through a sapphire crystal[44]. The white light maintains its temporal shape and coherence allowing picking of any desired wavelength within the WLC. The coupling from 800 nm pulse to WLC is however rather weak meaning the chosen output wavelength must be amplified. In order to amplify light of variable wave-length the three wave-mixing mentioned above is used.

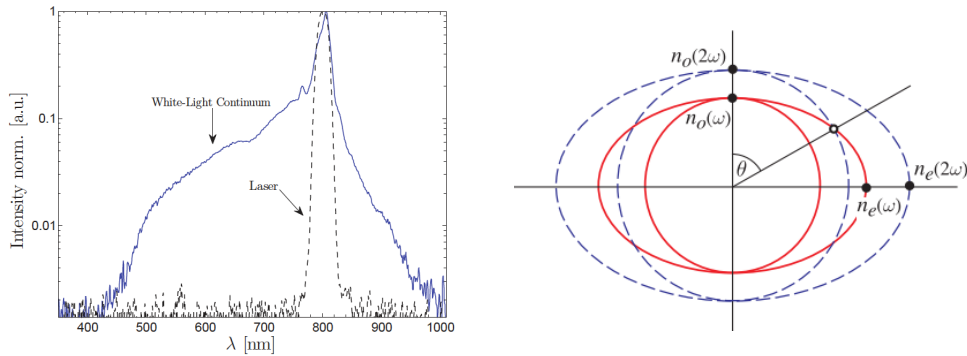


Figure 3.2: (left) shows the white light continuum created from a fs pulse with a central frequency of 800 nm, also show with a dotted line. Note that the intensities are normalised. (right) shows the phase matching criterion solved by a birefringent crystal. At a certain angle  $\theta$  the ordinary refractive index for the frequency doubled light matches the extraordinary refractive index at the original frequency, and the two beams will travel in phase through the crystal. Reprinted from [44] and [45]

Focussing on the SFG in three wave mixing, a light field of higher frequency  $\omega_3 = \omega_1 + \omega_2$  is produced. This process can be understood in the phonon description as two photons being annihilated to create one high energy photon and thereby ensuring energy conservation. The process can similarly be imagined running "backwards" so that one photon annihilates creating two lower energy photons. A challenge in all frequency conversion processes is dispersion. Since different frequencies experience different refractive indices coherence is lost and thereby effective conversion is spoiled. In order to maximize conversion phase-matching must be achieved, this can be expressed in terms of wave-number or refractive index as,

$$k_3 = k_1 + k_2, \quad (3.9a)$$

$$n(\omega_3)\omega_3 = n(\omega_1)\omega_1 + n(\omega_2)\omega_2. \quad (3.9b)$$

The phase-matching criterion should not be understood as a rigid entity but rather as a means of optimization, in the way that the intensity of the converted fields varies with the phase mismatch as a sharp sinc function[46]. One way of ensuring phase matching through the non-linear medium is by choosing a birefringent material. Birefringent materials possess both an ordinary and extra-ordinary refractive index, the latter being dependent on the optical axis of the crystal with respect to the penetrating beam. This method is best understood by figure 3.2 where the matching is done for SHG, making eq. 3.9 the much simpler  $n(2\omega) = n(\theta, \omega)$ . For a given angle the birefringent crystal will support the double frequency by the ordinary refractive index and the original frequency by the extraordinary. In that way phase-matching can be met by tuning the crystal angle, thus allowing conversion via SHG, SFG or DFG.

In practical use the tuning of angle, remixing and finally filtering away beams with unwanted frequencies is performed automatically, in this project by the TOPAS-prime and NirUV mixer from Light Conversion. These devices are computer controlled and has tuning curves with crystal angles embedded in the software allowing for a tuning range of 200-2000 nm when pumped by 800 nm pulsed laser light from the Solstice laser-system.

### 3.3 Optical setup

Once the ultra-short laser-pulse of the desired frequency is created it is sent through an optical set-up designed specifically for this experiment. The purpose of the set-up is to focus the beam, measure the pulse-energy of each pulse as well as providing an in-situ microscope giving the position of focus on the sample. All this should be done while maintaining the broad spectral width of the pulse as well as the narrow temporal pulse-shape. A figure of the optical setup is shown in figure 3.3.

To minimize losses at the mirrors, gold-coated mirrors are used in the entire 35 fs beam-line (red line on figure 3.3). In order to vary the energy the beam passes through a wheel of neutral density power filters (ND-filters) of varying strength. At two points along the beam pass the beam is split. An ordinary beam-splitter would distort and elongate the pulse due to group velocity dispersion (GVD), and hence so called pellicle beam splitters are used in both instances. Pellicle beam splitters excel for use with ultra-short laser pulses due to a membrane thickness of only  $2 \mu m$ , making GVD effect neg-

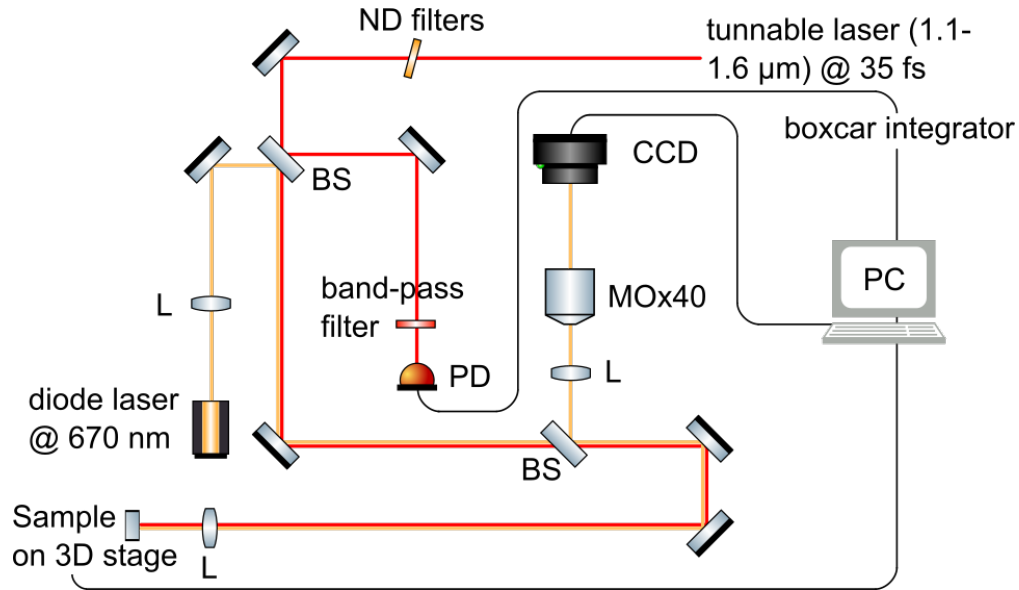


Figure 3.3: Shows the optical set-up build for near-field mappings. The red line indicates the beam-path of the fs laser while the yellow line indicates the beam-path of the imaging laser. Beam-dumps and apertures has been omitted from the figure for simplicity.

ligible. The splitting of both beam-splitters is 8/92 reflected/transmitted light.

The reflected 35 fs beam of the first beam-splitter is sent through a high-pass filter blocking all wavelengths below 1000 nm and into an InGaAs photo-diode responsive from 900 to 1800 nm (Thorlabs DET10C). This photo-diode is used for measurement of the pulse energy for each shot, more on this in the section *intensity calibration* below. The first beam-splitter is simultaneously used to couple in a CW laser at 670 nm for illuminating the sample. Before this beam joins the 35 fs beamline it is focussed by a lens with 350 mm focal length. This focal length corresponds to approximately a third of the distance to the sample, ensuring illumination of a spot-size considerably larger than the focus of the 35 fs beam at the sample. The second beam-splitter is only used for the light reflected off the sample, going back along the beam-line, as explained below.

In order to focus the 35 fs beam onto the sample a  $f=45$  mm achromatic lens is used. Before this lens two apertures has been placed ensuring alignment both into and away from the sample. Alignment away from the sample

should be understood as ensuring perpendicular angle of incidence via a two-directional tilt-stage and the reflection back through the before-mentioned apertures. The sample holder is a combination of a 3D-stage, the before mentioned tilt stage and a home build mount for SEM-sample holders. The 3D stage has two axes (up/down and towards/away from focus) controlled by stepper motors and one (horizontal perpendicular to beam) controlled by an air-bearing linear stage. All in all the sample is controllable to  $\mu\text{m}$  precision and perpendicular to the beam within a fraction of a degree.

The reflection off the sample traces back through the beam-line and is by the second beam-splitter reflected into a home-build microscope. The microscope consists of a lens similar to the one at the sample, thus creating an image of the focus in the focal-point towards the Microscope Objective (MO). This image is enhanced by a MO with 40 times magnification and recorded directly on a CMOS camera (Pixelink PL-D722). The microscope provides visual feed-back of where shots are fired, and by logging the distances with respect to a corner of the sample the areas of interest are easily found on Microscope and SEM for later analysis.

## Energy calibration

A crucial part of the experimental procedure in this thesis is knowledge of the exact pulse energy delivered to the sample. The laser system used is specified to have a variation in pulse energy of less than 1 %, this number however is for 5 kHz operation. For the use in this thesis the laser-system is sending a single pulse when triggered by computer control. This introduces thermal variations from pulse to pulse since the gain crystal in the amplifier does not reach equilibrium. Apart from this variation in the amplifier the TOPAS is possibly an even greater source of energy variation on single pulses. Due to the non-linear processes utilized by the TOPAS the conversion is extremely intensity sensitive. Secondly the crystals in the TOPAS and mixer are not temperature-controlled and thus there will be a warm-up shifting the phase-matching angle and conversion slightly. The resulting thermal build up is measured to be of a period of approximately 40  $\mu\text{s}$ .

In conclusion one cannot rely on measured average power or simply the amount of damping used in the beam-path. Instead single pulse energy measurements are done with the use of a photo-diode and a boxcar signal integrator. For this a fraction of the beam is sent into a photo-diode through a filter omitting all frequencies below 1000 nm, see fig 3.3. The signal

from the photodiode is fed to a Boxcar Integrator (BI), a NIM-BIN module capable of averaging analogue signal over a short time-span. The BI is triggered by the laser amplifier signal meaning a continuous 5 kHz rate locked to the pulse in time. Continuous triggering of the BI is chosen to avoid shifts in offset due to capacitor charging/discharging. Relative to the trigger a gate is chosen for integration of the incoming photo-diode signal. Since the rise and fall time of the photo-diode is approximately 1-2 ns a gate of 80 ns ensures that the entire signal is included with minimal noise. The output of the BI is a voltage drop varying from 0-1 V which is recorded to the computer with trigger timing from the laser output. Energy calibration can then be achieved by making coupled measurements with power-meter and photo-diode both averaging over several seconds for both. This provides a linear translation from photo-diode current to pulse-energy by dividing through with the repetition rate of 5 kHz. For photo-diode signals below 1 V (to prevent saturation) the correlation has a  $R^2$ -value exceeding 0.99.

---

## Experimental and characterization techniques

### 4.1 LabView program

As a part of the preparation for the near-field measurements most implementations of new equipment has required LabView programming for it to function properly together. Even though the program is merely a tool I have dedicated this section to document my LabView programming as it has been a part of my work for this thesis. All of the work done in LabView has been done expanding the existing program *Ablation Workstation* which already provided control of shutters, 3D stage and the "old" fs-laser.

#### Laser control

The solstice laser system is by default configured to produce a train of laser-pulses at variable rep-rate. For the use in this work single pulse operation is however essential. The Solstice is designed so that vertically polarized light is trapped in the amplifier. The optical path is such that the beam makes a double pass through a combination of a Pockels cell and a passive quarter waveplate. When the cell is off, the double pass through the passive quarter waveplate will flip the beam polarization 90 degrees whereas the on state leaves the polarization unchanged (180 degree flip). Single pulses can thus be extracted from the laser by controlling the pockels cells responsible for the pulse-picking from the stretcher into the laser amplifier. With a rep-rate of 5 kHz sending an "ON" signal of 200  $\mu s$  results in the laser picking only one pulse for amplification. Timing on this scale should not be software based as the execution time will depend on other processes running

on the computer since LabView is running on Windows parallel with other programs. For triggering the laser system a Digital Analogue Converter (DAC) with a built in clock-frequency is used. Through the DAQmx sub-vi package this DAC is configured to deliver TTL pulses at 2 V of 200  $\mu s$  duration by the push of a button or as part of an automatized action (the number of pulses is written on the user interface and multiplied by 200  $\mu s$ ). Further an "always on" feature is added by setting the TTL signal high indefinitely giving the opportunity to align the optical set-up with the laser running continuously.

## Program features

- **Focus Find**

Despite being labelled as an achromatic lens the focus distance changes with wavelength by approximately 1 mm going from visible to telecom (1550 nm) wavelength. Furthermore the focal length of 45 mm is not related to any motor-positions on the 3D stage since target thickness and mounting changes. This calls for a precise way to determine the exact position of focus on the z-direction, parallel to the incoming beam. By scanning over z-distance the sample is moved in and out of focus. At each step the sample is moved in either x or y-direction and a selected number of pulses is fired. The z-value corresponding to the focus of the wavelength in question is found by inspecting the ablation craters either in-situ on the home built microscope or subsequent on optical microscope or SEM. Since the pulse to pulse variation is quite high for single pulses through the TOPAS single pulse alterations provide poor information of the focus-position. Single pulse measurements would provide the opportunity to compensate for this but the extensive data analysis accompanied by this makes it impractical. To overcome this problem bursts of 50-100 pulses are used instead giving a much more steady mean pulse energy. 50-100 pulses are chosen since this gives a standard derivation of approximately 5 % of the mean pulse energy. The use of pulse-bursts rather than single pulses of course introduces incubation effects resulting in a threshold fluence much lower than for single pulses. The focus finder additionally has a function creating a mark shot containing more laser-pulses at the first spot which ensures correct hole-count should the focus find start off-focus at an extend of no material change. For practical ease of use the direction of travel in the x/y can be chosen as well as centering the z-variation around the current z-value.

- **Pulse-energy measurements**

The output signal from the boxcar integrator is read into the Ablation Workstation via an input on the same DAC used for triggering the laser. Since the BI is continuously triggered the read-out must happen with 200  $\mu s$  after the pulse (due to the 5 kHz rep rate). This timing is assured by using the synchronization output from the Solstice laser-system as a trigger for energy read-out. The sync-out produces a TTL signal  $\sim 3 \mu s$  before the laser-pulse reaches the photo-diode (sync signal is sent when the amplifier receives the seed pulse). Since the DAC has an onboard clock capable of 1 MHz sampling, readout at  $\mu s$  timing is easily achieved. To avoid recordings of the risetime of the boxcar integrator 20 samples are recorded, subsequent taking the 10th value. In addition to single pulse measurements an option to average photo-diode signal with the laser running at 5 kHz is made. Since this should average over several seconds and the laser energy is rather stable (meaning no problem with BI rise time) the sampling procedure is slightly different. For each pulse 2 samples are recorded with the second sample being sent to an array. This array is then normalized according to the number of seconds defined for the measurement. Both averaged photo diode signals and single pulse measurements are sent to an array for display in the program. This energy-display can be reset by the user, as well as saved to a text-file.

- **Energy Calibration** Based on the pulse measurements described above an energy calibration must be made in order for the photodiode signal to make any sense physically. The calibration is done by averaging for the same number of seconds on both the photo-diode and a thermocouple power-meter. The dependency is linear and a least squares fit is made when the desired number of data-points has been collected. There is an option showing plot of the data-points along with the fit obtained, as well as an option to subtract the background level measured by the power meter. Finally one has the option to apply the fit to future pulse-measurements for easier comparison of pulse energies across wavelengths, as well as saving to a text-file.

## 4.2 Imaging techniques

### Optical microscopy

Since the most evident change in GST is the surface reflectivity at optical wavelengths conventional Optical Microscopy (OM) offers great phase con-

trast. Ablation is naturally also easily seen on optical microscopes making the conventional optical microscope well suited for characterization of the laser-beam in the ways of focus size, beam profile and threshold determination. For investigations of plasmonic effects the resolution is however far too low, primarily due to the diffraction limit as explained below.

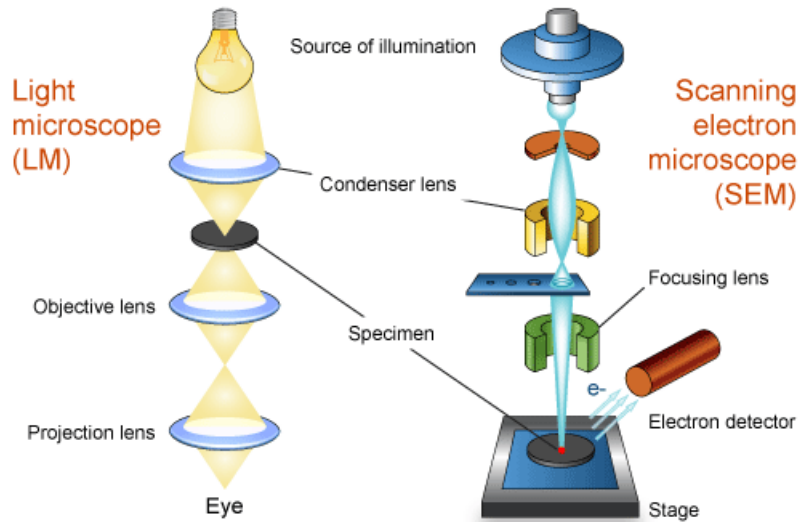


Figure 4.1: Shows a comparison of basic layout of an optical microscope (left) as compared to a scanning electronic microscope (right). Reprinted from [47]

An optical microscope typically consists of two lenses to provide tunable magnification. The working principle is shown in figure 4.1, compared to an electron microscope which is used for investigating features below the range of the OM. The microscope used in this project offers magnification up to a thousand times, making features larger than  $\sim 5\mu\text{m}$  resolvable.

In addition to the commercial OM a home build microscope is part of the experimental platform for in situ imaging of the sample. The magnification of the home build microscope is a factor of 40 however with the enlargement of the Full-HD camera from CMOS chip to screen a combined magnification of 800 times is achieved (somewhat arbitrary number since it depends on the screen resolution and size of the video-preview). The resolving power of this microscope is practically limited by an overlaying diffraction pattern since it is illuminated by a 635 nm laser. The choice of a coherent light source should generally be avoided, however the challenge here is to couple

enough light into the beam-path through the poorly reflecting pellicle beam-splitters.

### The diffraction limit

In broad terms diffraction can be defined as the bending of light around obstacles. The obstacle responsible for the diffraction in the case of diffraction limited microscopes or focusing is the circular lens, giving a Fraunhofer diffraction of intensity with [37],

$$I(r, t) = I_0 \left[ \left( \frac{\pi a^2}{\lambda z} \right) \frac{2J_1(2\pi ar/\lambda z)}{2\pi ar/\lambda z} \right]^2, \quad (4.1)$$

where  $a$  is the radius of the lens/aperture,  $z$  the distance from the object and  $J_1$  the first order Bessel function. This is often called an Airy pattern, and has a number of nodes along  $r$  where the intensity drops to zero. The first such point is at,

$$r = 1.22 \frac{\lambda z}{2a}, \quad (4.2)$$

and serves as a clever measure of the smallest distance between two objects that the system can resolve, the Rayleigh criterion. In numbers the Rayleigh criterion is the point where the dip in intensity between two airy extrema is 20 % lower than the two maximum intensities. For microscopes this criterion is conveniently expressed in terms of the numerical aperture giving the formulation[43],

$$d_{OM} = \frac{\lambda}{2n \sin(\theta)} = \frac{\lambda}{2NA} \approx \frac{\lambda}{2.8}. \quad (4.3)$$

For one thing this means that at optical wavelengths one cannot resolve features smaller than roughly  $0.2\mu m$ . In addition the same considerations are valid for focusing the laser beam. Assuming a gaussian beam profile a relation similar to equation 4.2, is valid for focusing. For lasers the beam divergence ( $\phi$ ) is determined by the cavity design through the beam diameter in the cavity  $D$ [43],

$$\phi = \frac{1.27\lambda}{D}.$$

The focusability of a laserbeam is then found to be,

$$d_{Laser} = f \frac{1.27\lambda}{D}. \quad (4.4)$$

Here  $f$  is the focal length of the lens used for focusing. The beam waist of the TOPAS beam is 11 mm and is focused by a 45 mm lens. By equation

4.4 this corresponds to a minimal spotsize of  $7.8 \mu\text{m}$  for  $1500 \text{ nm}$  light in the focal plane.

## Scanning Electron Microscopy

Scanning Electron Microscopy (SEM) shares many similarities with optical microscopy in working principle, but has significant advantages as well as disadvantages when it comes to imaging of GST-changes. SEM greatest advantage is ultra-high resolution easily surpassing the optical microscope as SEM is capable of resolving features of nm-size. This ultra-high resolution is a direct cause of using electrons as source. Electrons can rather effortlessly be accelerated to keV energies, resulting in a de-Broglie wavelength of  $17.3 \text{ pm}$  for a  $5 \text{ keV}$  electron. With wavelengths in this scale, the diffraction limit is no longer a limitation for nm-scale microscopy and modern SEM's are capable of continuous magnification down to nm scale (continuous in the way that you can go from 10 to 500 000 times magnification on the same machine)[48].

A sketch of the central components of a SEM can be seen in figure 4.1 where it is shown in relation to an optical microscope. The electron source is typically made from wolfram which emits thermal electrons at high temperatures, but other materials can be used as well as field emission guns[49]. The SEM used for this thesis is a Nova NanoSEM 600 from FEI and has a field emission gun as electron source. The electron beam is condensed and focused onto the sample using two or more electromagnetic lenses which also perform the scanning over the sample. Due to the charge of the electrons, control and focussing of the beam is precise and adjustable by electromagnetic coils. As the electron beam is focused onto the sample, the electrons penetrate through the surface creating a droplet-shaped interaction volume. The re-emitted radiation corresponds to the region of origination in the way that low energy secondary electrons (few eV) originate from the surface (nm depth) whereas backscattered electrons of higher energy (keV range depending on incident energy) originate from deeper within the sample ( $\sim 100 \text{ nm}$ ). Finally x-rays can be detected as well giving an even larger interaction volume ( $\mu\text{m}$  depth). In most cases the interaction volume is the limiting factor as opposed to the optical microscope where the diffraction limit and lens quality restrains the resolution.

### GST phase-contrast on SEM

Contrast with secondary electrons (SE) are based on a variation of the number of emitted electrons with angle of incidence. More SE escape from steep surfaces making these brighter on the SEM image. When scanning over the sample this creates topological information of the surface. SE are thus ideal for imaging ablation and gold nano-particles down to nm resolution but not very well suited for GST phase changes since only a small swelling of the amorphous phase is observed as mentioned in section 2.3. Furthermore the continuous irradiation from the electron contaminates the samples creating dark artefacts. Since the phase-change only appears as slight contrast variations this shadowing makes phase-change imaging on SEM tedious.

Another possibility is imaging with backscattered electrons. In this mode the detector is given a negative bias to repel the low energy secondary electrons, and instead obtain a signal of high energy electrons returning after one or more scatterings in the sample. Since backscattered electrons have a larger contact region lower resolution is obtained. The advantage of imaging with backscattered electrons is that the signal is more influenced by material parameters such as density and crystal lattice. This results in a rather good detection of phase difference between amorphous and crystalline GST at the cost of resolution on the nm scale. A comparison of the ablation and phase-change contrast on OM and SEM can be seen in figure 4.2.

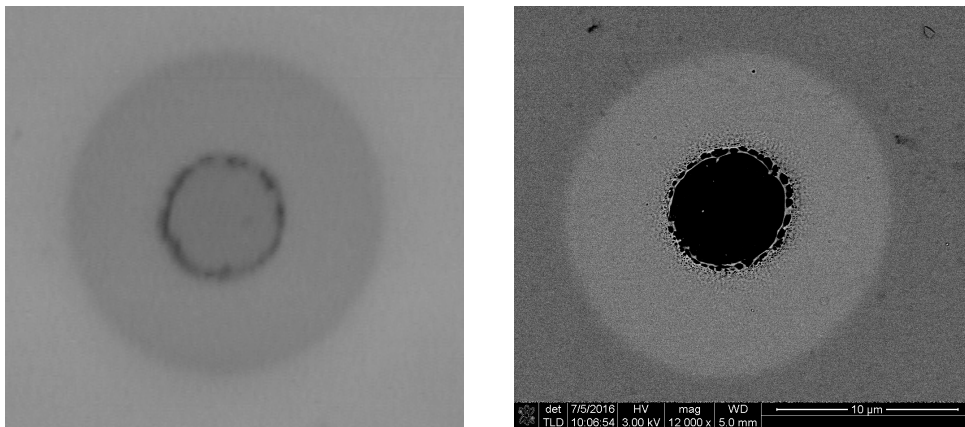


Figure 4.2: Shows the the same hole as seen in the optical microscope (left) compared to the electron microscope (right). The optical microscope is at maximum magnification for this picture. The SEM image is obtained with backscattered electrons from an electron beam at 3 kV and a spot size of 5.2

The contrast with backscattered electrons is very sensitive to equipment parameters and thus the right combination of spot size and electron energy was not discovered until June 2016. This means that for some of the early experiments detection of the phase change has not been available below  $5\ \mu\text{m}$  due to the diffraction limit of the optical microscope. A publication by the group of Jan Siegel in Madrid [21] shows some promise towards obtaining high resolution SEM contrast, using secondary electrons.

Preliminary investigations towards AFM detection of phase contrast has been made. For a GST film thickness of 40 nm the density difference of 6 % [36] leads to a swelling of only 2.4 nm. With tip-sample convolution and subsequent digital image flattening this small difference is easily lost in image artefacts giving no significant advantage over SEM. Some reports of nano-meter phase contrast by using conductive-AFM has been reported in e.g. [50]. This has not yet been pursued due to the success of SEM imaging with BE combined with the massive tip-sample convolution expected around the nano-particles. There is however the possibility to remove the nano-particles after irradiation. In conclusion then the phase contrast at sufficiently high resolution remains a challenge in this project. Much progress has been made up to the time of writing this thesis with SEM using backscattered electron being the best technique at this time.

### 4.3 Sample preparation

All of the near-field studies in this project is made on GST thin films due to the phase-change ability along with the relatively low ablation threshold. These thin-films were deposited by radio frequency magnetron sputtering, and subsequent equipped with nano-particles on top. The sputtering process has been a part of my work for the project whereas the electron beam lithography producing the gold nano-particles are made by other members of the SunTune project.

#### Magnetron sputtering

The Radio Frequency (RF) magnetron sputtering is performed in a vacuum chamber, where the sample is mounted opposite to a target with the desired deposition compound, here GST. Plasma is created in the chamber from a noble gas, in this case argon. The plasma is initiated by stray electrons accelerated by the RF-field ionizing the argon atoms, thus creating a cascade effect of ionization resulting in a plasma. Due to the rapid switching

of the polarity only the electrons can keep up with the field, leaving the argon ions trapped mid-cavity. By setting a negative charge on the targets a bombardment of argon ions hits the target freeing a vapour of GST off the target. The freed material will form a thin film on the sample which is rotated to give a uniform coverage. By placing permanent magnets in the chamber the plasma is further confined immediately above the target ensuring high deposition rate.

The deposition can be adjusted by tuning the RF-voltage, Argon pressure, target bias and substrate temperature. For the deposition of the GST thin films a commercial ATC Orion RF-MS system from AJA International was used. The GST was grown at room temperature, with an Argon pressure of 3 mTorr and a power of 100 W. Through calibration of the deposition rate, GST-layers of 40 nm's thickness has been created on top of both Silicon and Quartz. The thickness of the layers was confirmed by profilometer and SEM measurements.

The method of deposition results in a GST thin-film that is likely amorphous or partially crystalline. Since ultra-short pulses only support shifting from crystalline to amorphous, subsequent annealing of the GST-samples is performed to ensure crystallization. Annealing at approximately 600 to 650 K GST solidifies in the hexagonal structure whereas annealing at 450 to 500 K results in the FCC structure[51]. The samples were annealed at 500 K since the FCC of GST structure is much easier shifted from crystalline to the amorphous phase, allowing for fast switching by femtosecond laser-pulses. The crystallization was confirmed by making XRD measurements of a sample before and after annealing. This clearly showed peaks corresponding to the crystal lattice (with (200) and (220) being most distinct) for the annealed sample whereas the sample directly from sputtering only showed remnants of the Silicon underneath the GST thin film.

## **Nano particle deposition**

Since the goal of this project, is to measure the near-field of nano-particles, a flexible method for shaping particles down to nm accuracy is needed. Electron Beam Lithography (EBL) is the method of choice and it offers full 2D control of feature-sizes below 5 nm. The method achieves this high resolution exactly like the SEM by irradiating with electrons, since they are easy to focus and control and have a short wavelengths. In fact the method of operation is so similar that some EBL-equipment is build exactly as the

SEM shown in fig 4.1 up until the specimen. For EBL the electron beam writes the desired pattern on a special coating (called the resist) which changes solubility upon radiation. Areas exposed, or not exposed according to the tone of the resist, are removed chemically. After removal of the exposed resist the substrate of the nano-features is deposited across the entire sample sitting on top of the resist at non-irradiated areas and on top of GST at the exposed areas. Final removal of the remaining resist leaves gold only at the exposed areas, resulting in gold nano-particles of the desired size and shape. It should be made clear that the deposition of nano-particles are not done by me, but performed by Adnan Nazir who is a postdoc also associated with the SunTune project.

A general artefact of EBL is a slight truncation of the structures. Since the LSP's are extremely sensitive to even the slightest change in geometry (as discussed in section 2.2), this effect must be considered. In order to get a fair ground for comparison, the nano-particles should therefore be measured by AFM or SEM in order to do the modelling on realistic particle geometries.

### Particle dimensions and pattern

The experimental work in this project has been performed on two different particle configurations. As mentioned in section 2.2 both the size shape and pattern has significant influence on the enhancement factor as well as the resonant wavelength.

The first experiments where conducted on gold discs. These where oriented randomly with a particle density of 2.9 %. The nano-discs are attractive to work with in the way that they are simple in geometry, making simulation easier. Discs are also quite similar to the spherical geometry where analytical solutions are available. This means that a near-field resembling the dipole solution for spheres is expected. The downside of nano-discs is that the field enhancement is not very sharp and pronounced. The nano-discs have a diameter of 245 nm and a height of 50 nm. The random ordering should dampen the coupling between the particles meaning that the particles can be assumed as "alone" on the sample while the particle density is still high enough to hit multiple particles with one laser-pulse. A SEM picture of the nano-discs is shown in the left panel of figure 4.3.

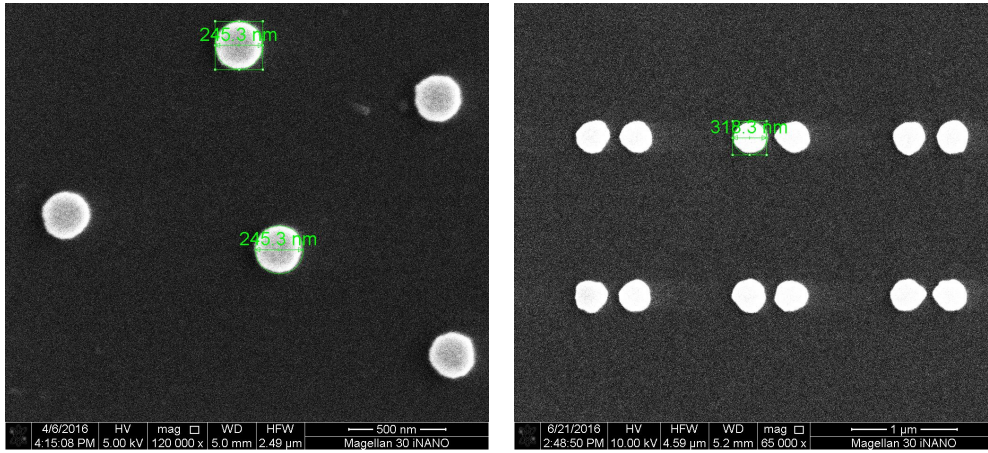


Figure 4.3: Shows SEM images of the two NP-geometries investigated for this thesis.

The final investigations made for this thesis is conducted on a periodic array of gold disc pairs. The nano-discs are 320 nm in diameter and have a height of 50 nm. The gap between the pairs is 770 nm along the joint axis of the two discs and 1200 nm in the perpendicular direction (both measured from the closest points). A SEM picture of the structure is shown in the right panel of figure 4.3. Due to problems with the EBL equipment the nano-particle deposition could not be done in the regular way of stitching smaller areas of nano-particles together to achieve a larger covered area. Instead the irradiation was performed in a single stage position at maximum beam scanning angle. This gives a change in the incidence angle of the beam resulting in distorted structures away from the central position. A clear evidence of this is the separation between the two adjacent discs which varies from 50 to 100 nm.

This irregularity naturally limits the ability to compare shots at different positions on the 500 by 500  $\mu\text{m}$  array of nano-particles. The structure does however feature a number of advantages to single discs above. The symmetry means that the LSP will be sensitive to the polarization direction of the light. The array formation further introduces two characteristic distances giving resonances corresponding to the on/off axis distances between the nano-disc pairs. Also the gap between the particles in the NP-pair is within the working range of the plasmon hybridization model, allowing analysis based on this.

---

## Experimental work and data-analysis

### 5.1 Short pulse excitation of GST

An absolutely critical parameter in the experimental work for this project is the fluence threshold for the phase-change and ablation of GST. Mainly because the enhancement factor is defined in relation to these threshold values but also because they are used as fitting parameters when back-tracking the field strength at certain points near the center of the pulse. The threshold values are measured directly in the next section using the  $D^2$ -method. The threshold values as a function of wavelength can alternatively be estimated from the complex refractive index  $\underline{n}$ . Ellipsometry measurements provide both the real and imaginary part of the refractive index at wavelengths spanning from 350 to 2500 nm. The absorption coefficient is highly dependent on the wavelength both explicitly and through the imaginary part of the refractive index. The absorption coefficient for absorption according to Beers law is given by,

$$\alpha = \frac{4\pi\kappa}{\lambda}. \quad (5.1)$$

Where  $\kappa$  is the imaginary part of the refractive index  $\underline{n} = n + i\kappa$  and  $\lambda$  the wavelength. Absorption according to Beers demands an exponential attenuation with a characteristic absorption length  $1/\alpha$ . In figure 5.1 the key optical parameters are shown as a function of photon energy.

The data found for figure 5.1 shows good agreement with optical parameters reported in [52], a study of the absorption coefficient in the three GST phases. The necessity for a chromatic investigation of the optical properties

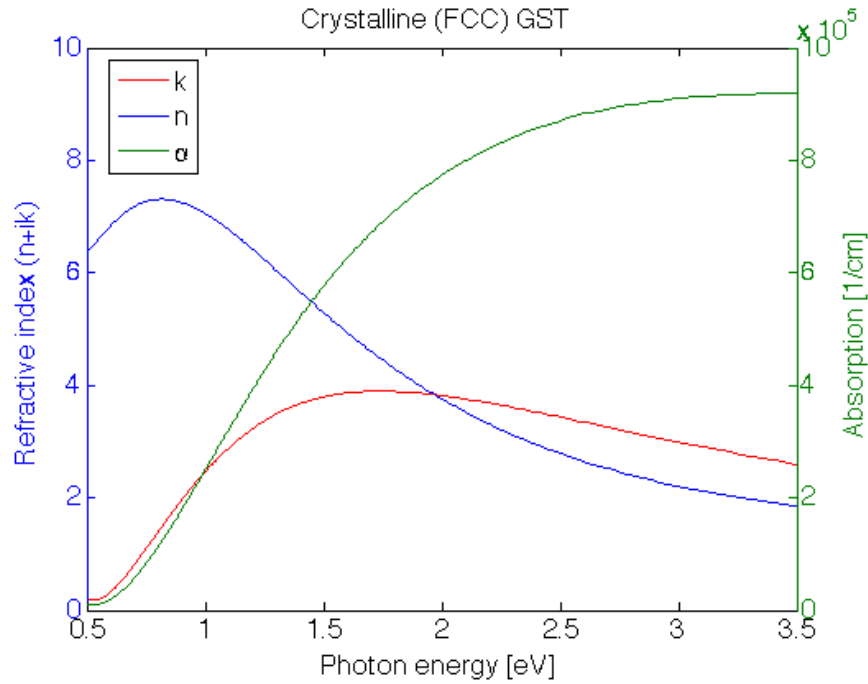


Figure 5.1: Shows the optical parameters of GST as a function of photon energy. The data is obtained from ellipsometry measurements. Notice the considerable changes right around the region of interest for the SunTune project (0.8 to 1.1 eV) indicating a high variation of material response with wavelength.

of GST is quite evident from the refractive index and absorption coefficient in the region of interest for this thesis (1100-1600 nm corresponding to 1.1 to 0.8 eV). The optical parameters are used for giving an estimate of the wavelength dependency of the phase-change and ablation thresholds as well as used for the numerical near-field simulations made by other members in the SunTune project.

From the measured absorption coefficient  $\alpha$  it is possible to give an estimate of the threshold energy required to melt the crystalline GST and thereby switch to the amorphous state. Assuming absorption according to Beer's law the energy deposited in a volume can be related to the irradiation as [12],

$$F_{th} = \frac{\Delta H}{\alpha A}, \quad (5.2)$$

where  $\alpha$  is the absorption coefficient,  $A$  the absorptance and  $\Delta H$  the en-

thalpy required for heating, melting and in the case of ablation also enthalpy of evaporation. The enthalpy required for phase-change and ablation can be expressed explicitly as,

$$\Delta H_{PC} = \rho_s C_{p,s} \Delta T_m + H_{Fusion}, \quad (5.3a)$$

$$\Delta H_A = \rho_s C_{p,s} \Delta T_m + H_{Fusion} + \rho_l C_{p,l} \Delta T_b + H_{Vap}. \quad (5.3b)$$

Here densities  $\rho$  and specific heat capacities  $C_p$  for the solid  $s$  and liquid  $l$  material is used. The calculations from Beer's law is hardly more than an estimate. The calculation is however instructive in exposing the physics behind the excitation and will serve as an guideline for the wavelength dependency and order of magnitude of the threshold material alterations.

## Fluence threshold determination

In order to experimentally determine the threshold values for ablation and phase change a series of single shot irradiations with varying pulse energy is made. At sufficiently low irradiation the intensity is not high enough across the entire spot size to melt and thereby switch or ablate the GST sample. Assuming a gaussian intensity distribution the diameter of the melted region is instead given by [12],

$$D^2 = 2\omega^2 \ln \left( \frac{E_{pulse}}{E_{Th}} \right). \quad (5.4)$$

Here  $\omega$  is the spot-size of the beam and  $E$  denotes the pulse-energies summed over both temporal and spatial distribution. Equation 5.4 holds true assuming that there is no heat diffusion and that the melting occurs at a specific threshold energy.

This expression is particularly convenient when plotted on a logarithmic energy axis. The threshold pulse energy is found simply as the intersection  $D^2 = 0$  and the spot-size of the beam as the slope of the curve. The beam profile is distorted after the passage through the TOPAS, resulting in an elliptical focus at some wavelengths. An aperture is introduced at the output of the TOPAS to correct this error however, since the beam is cut to a minimal degree elliptical beam shape is still present at some wavelengths. In cases with an elliptical beam profile the two lines are fitted to a common threshold value, whereas cases with no apparent longer axis are fitted simply to a single line corresponding to the diameter of the beam profile. An

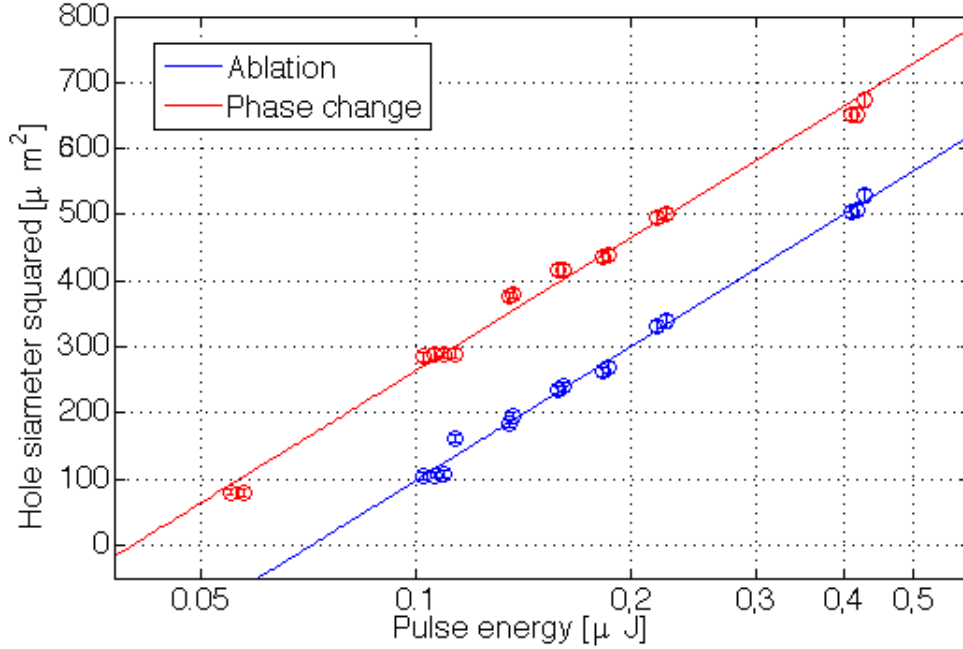


Figure 5.2: Shows how the size of the ablated and phase-change areas increase with pulse-energy on a logarithmic energy scale. The fit to both data-sets is on the form of eq. 5.4, so that the intersection with the energy  $E_p = 0$  marks the threshold energy and the slope corresponds to the spot-size.

example of a threshold measurement taken at a central wavelength of 1300 nm is shown in figure 5.2

The threshold energy found by fitting to equation 5.4 as illustrated in figure 5.2 is naturally related to the focus through the spot size and thereby a poor quantity for comparison. A more suitable unit of measure is the fluence, found through the relation [53],

$$F_{th} = \frac{2E_{th}}{\pi\omega_{maj}\omega_{min}}. \quad (5.5)$$

It should be noted that the threshold fluence is still dependent on pulse duration. An example of this is shown in [54] where threshold values are experimentally determined to be 10.32 and 5.30  $mJ/cm^2$  for 30 ps pulses and 23.98 and 11.6  $mJ/cm^2$  for 8 ns pulse duration. However since all of the work done for this project is performed with 35 fs pulses from the same laser system, no further investigation of this dependency has been made. In order to investigate the wavelength dependency of the threshold fluence measurements similar to the one shown in figure 5.2 are made for

a variation of central laser wavelengths. As argued above in reference to changes in absorption coefficient and refractive index, the threshold fluence is also dependent on the wavelength of the radiation. A comparison of the crude approximation from Beer's law with experimental values at varying wavelength is presented in figure 5.3.

For the solid line in figure 5.3 the absorptance in equation 5.2 is found as a function of wavelength by Fresnel's equations based on the ellipsometry data. The density  $\rho$  and the heat capacity  $C_p$  is taken to be ( $5.995 \text{ g/cm}^3$ ) and ( $218 \text{ J/kgK}$ ) respectively as found in [55]. Combined with a melting temperature of  $618 \text{ }^\circ\text{C}$ [56] the heating term given. The enthalpy of fusion is found to be  $610\text{-}625 \text{ J/cm}^3$  in [57]. Resulting in a critical energy density of  $1397.6 \text{ J/cm}^3$  for permanent phase-change to happen. No values for the enthalpy of evaporation is not documented since melting is the phase change of main interest in GST.

As seen in figure 5.3 the threshold fluence is clearly higher at infra-red wavelength, however the agreement with Beer's law is not entirely convincing. As argued in section 2.3 this is expected since the absorption might very well be non-linear to a degree determined by wavelength. The approximation does however succeed in foreseeing the rate of increase in threshold fluence. Another observation about the data is that the ablation threshold is steadily 1.8 times greater than the threshold fluence of indicating that the combined energy density required for heating the GST to the boiling point and subsequent evaporation, is approximately  $2500 \text{ J/cm}^3$ .

## 5.2 Near-field patterns

When describing the observations regarding nanoparticle plasmon enhancement two scales are generally used. On the micrometer scale the impact purely from the laser-pulse is seen. This amounts to two boundaries marking the threshold fluence for ablation and phase-change respectively. The circular or elliptical contour lines are used for determining the laser fluence incident at any point near the pulse center via a gaussian fit. Due to the diffraction limit no features below approximately  $5 \mu\text{m}$  can be the result of laser induced damage. The effects near the nano-particles is described on a nanometer scale. The incident laser fluence is taken to be constant at the position of a given nano-particle and any material alterations on this scale are a result of near-field enhancement by the localized surface plasmon.

For nano particles in a region of sufficiently high laser fluence, regions with

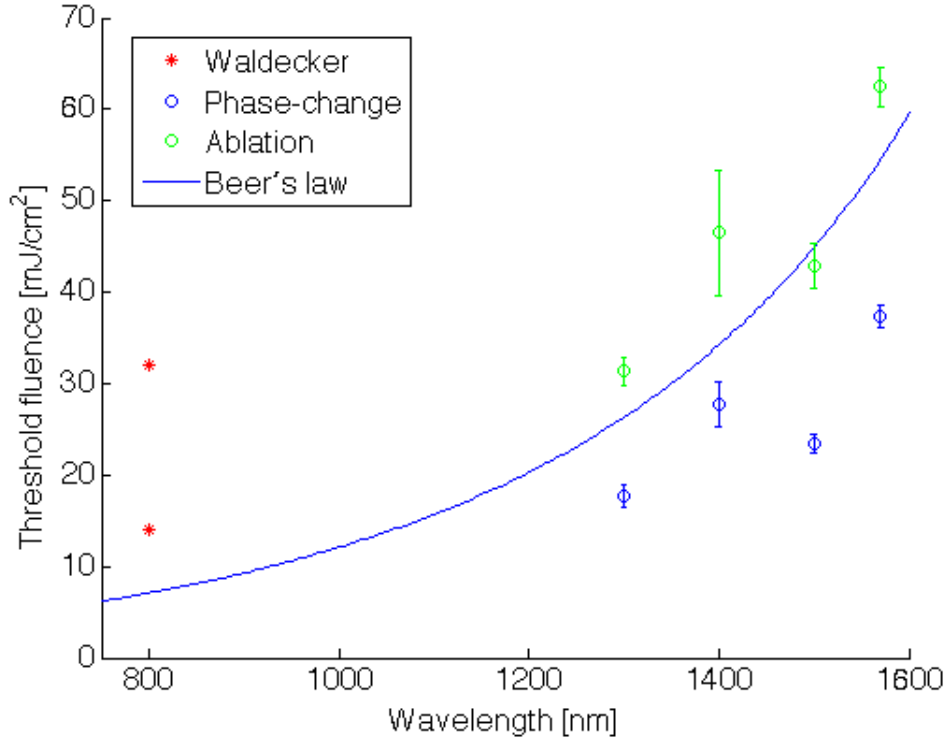


Figure 5.3: Shows the laser-fluence as a function of laser wavelength. All data-points are experimental values achieved by excitation with 35 fs pulses. The solid blue line shows the approximation using Beer's law describing the absorption. The red datapoints at 800 nm is ablation threshold 32 mJ/cm<sup>2</sup> and phase change at 14 mJ/cm<sup>2</sup> with 35 fs laser as found by Waldecker et al., [25].

ablation near the nano-discs appear. An example of this for a central wavelength of 1300 nm is shown in the left panel of figure 5.4. The dark region corresponds to the bottom of the ablation crater whereas the bright region away from the NP corresponds to the steep edge of the ablation crater combined with material swelling due to the rapid heating. Apart from field enhancement at the two poles of the NP additional "wings" of field enhancement is observed. Since the enhancement factor in these "wings" is quite low they can only be found very close to the boundary of laser induced ablation or phase change. At these locations the field enhancement at the position of the NP is so high that the particle is expelled and thus a good picture of both effects simultaneous cannot be presented. The NP in figure 5.4 is situated in a region with sufficient laser fluence to switch the GST

phase by pulse radiation and thus no near-field features are seen by phase contrast. This is remarkably still the case for NP's situated in just below the phase change threshold fluence. Ablation may still be present but no phase change is seen near the particle. Only the wings of field enhancement further from NP are observed to induce a phase shift, however only at 1350 nm where this feature of the near-field is most pronounced.

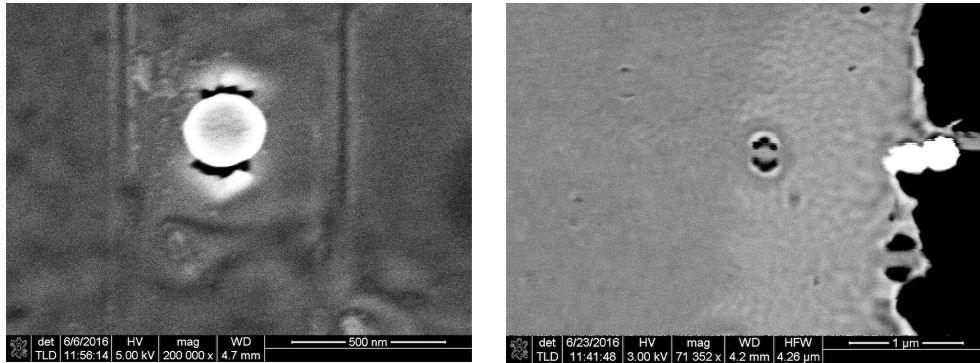


Figure 5.4: Shows SEM images of the nano-particles after laser pulse radiation. To the left is a close-up of a nano particle inducing ablation at its poles. To the right the effects of the nano-particles to the nearby GST is shown, this image is taken after manual removal of the nano-particles.

For the array of nano-disc pairs, nano-scale phase change is however clearly present. Figure 5.5 shows two pairs of nano-particles situated just outside the boundary of laser induced phase change. No ablation is present, but the "wings" underneath the the two lowest particles resemble the features seen on the single particles. In the region between the two NP pairs an even bigger area of amorphous GST is seen.

### Heat reservoir explanation

The full explanation behind the absence of phase shift near the NP's is not known and no mentions of it has been found in the literature. A possible explanation is that the gold particle acts as a heat reservoir obstructing the rapid heat dissipation critical to the switching ability of GST. This explanation is proposed on the grounds of the observations made for this thesis and discussions primarily with Søren H. Møller about the origins of the unchanged GST zone around the NP's. The melting temperature of GST is 891 K while the crystallization to the FCC structure happens down to temperatures of 450 K [56, 51]. The crystallization time of GST is 500 ps[35].

The gold should thereby be able to maintain a temperature elevated above 450 K on this time scale for it to cause the re-crystallization. To do so the gold particles must attain sufficient thermal energy from direct absorption and heat transfer from the surrounding GST. To assess whether the heating of the nano-particle is a valid explanation an estimate of the temperature increase and "lifetime" of this thermal energy storage is instructive. From simulations of the nano particles in question the absorption cross-section is found to be in the order of  $10^{-15}m^{-2}$  at the wavelengths of the interest. Assuming a laser-fluence of  $40mJ/cm^2$ , corresponding to just below the ablation threshold, the energy absorbed in the nanoparticle is 0.4 pJ. By taking into account the particle dimensions and the heat capacity of gold this absorption results in a temperature increase of 68.2 K. Absorption alone is evidently not able to heat the NP by the 150 K needed. Another source of the heat is thermalization with the GST layer. High thermal conductivity is at the very core of the mechanism allowing for phase change, normally in the way that the heat is absorbed by the underlying silicon before the GST crystallizes leaving the sample amorphous. Gold has a thermal conductivity more than double that of silicon, 318 vs 149  $Wm^{-1}K^{-1}$  [58, 59]. Without giving any specific numbers it is reasonable to assume that the gold particle will be heated by the surrounding GST to a final temperature above 450 K, including the heating from direct laser absorption.

Another aspect is of course the "lifetime" of the temperature increase. The energy loss by radiation corresponds to less than  $1\mu K$  in temperature difference over the 500 ps needed for crystallization. Heat flow from the nano-particle to the underlying GST is a more complicated matter to describe due to the scale of the gold particle. In a study by Zhdanov published in 2012 [60], a model is proposed describing the heat transfer between metal nano-particles and supporting nano-layers. In this phonon-mediated model the heat transfer coefficient  $\alpha$  is given by,

$$\alpha_{Au,GST} = N \cdot \frac{3\pi A^2 k_B}{2m_{Au}m_{GST}\omega_D^2}, \quad (5.6)$$

where  $N$  is the number of contacts on the interface,  $A$  the interaction term and  $\omega_D$  the Debye frequency of the body delivering heat. The interaction term is in the article by Zhdanov estimated to be  $0.2 eV\text{\AA}^{-2}$  with Au nanoparticles on *Si*, *Fe<sub>2</sub>O<sub>3</sub>* and glass, this value is assumed to be reasonable for Au on GST as well. For the mass of GST the weighted average of the atomic components is used and the number of contacts is assumed to be

$2 \cdot 10^{19} m^{-2}$ . The Debye frequency of gold is found by,

$$\omega_D = \left( \frac{3N}{4\pi V} \right)^{1/3} v_s, \quad (5.7)$$

where the speed of sound  $v_s$  and the number density of atoms  $N/V$  is material properties for gold[59]. The thermal transfer coefficient is found to be,

$$\alpha_{Au,GST} = 1.78 \cdot 10^6 W m^{-2} K^{-1}.$$

For a single nano-particle at a temperature elevated 200 K above that of the GST film the energy flow then becomes,

$$\Delta E = 1.675 \cdot 10^{-5} W.$$

Corresponding to a decrease in nanoparticle temperature at a rate of,

$$\Delta T = 2.142 K/ns.$$

In conclusion there is no direct evidence against the heat reservoir explanation as the numbers are in good agreement with the temperatures needed and could be sustained long enough for the GST to re-crystallize.

In the right panel of figure 5.4 evidence supporting the heat reservoir theory is seen. The image is obtained using backscattered electrons in SEM giving a high contrast between the GST phases. To the right the boundary of the ablation crater is seen and in the band of a-GST (brighter than the c-GST) it is clearly seen that a circle around the NP is kept crystalline. Since the nano particle has been removed for this image any doubt is cleared on whether the absence of phase change around NP's is merely an artefact of SEM. The observations in figure 5.5 regarding NP's in an array is in agreement with the heat reservoir explanation as no phase change is seen near the NP's in this case either. There could however still be other valid explanations of this behaviour, and one should be cautious in concluding too much from this theory.

### 5.3 Quantitative near-field measurements

In order to determine the field enhancement of the nano-particle geometry the fluence at each specific NP must be known. From threshold measurements the threshold fluence for ablation and phase change is well known at

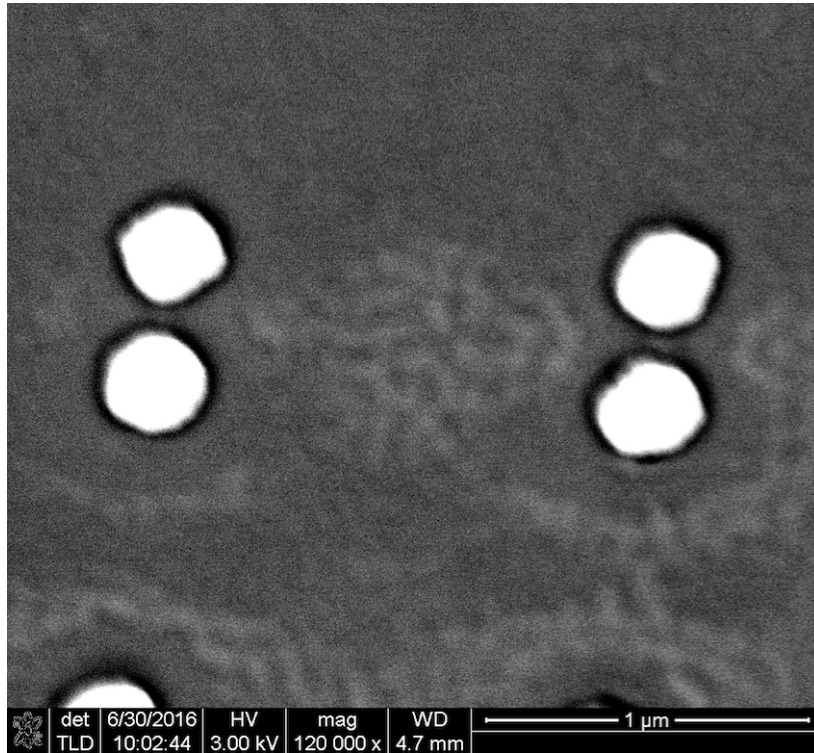


Figure 5.5: Shows two pairs of nano-particles situated just outside the boundary of laser induced phase change. The polarization is along the joint axis of the nano particles constituting the pair.

all relevant wavelengths. This provides the basis for fitting a gaussian field distribution to the contour lines corresponding to respectively the phase change and ablation boundary. To adjust for the possibility of an elliptical pulse shape the data is rotated to align the eccentricity with one of the principal axes. In figure 5.6 the conversion from SEM picture of a hole in the GST to a gaussian fluence distribution is shown. The positions of the nano-particles investigated is recorded and by the fit converted to a local fluence at the exact spot of the nano-particle.

An alternative procedure to this could be to use the pulse energy measured experimentally and then reconstruct the pulse from this energy. This does however not directly take the pulse shape into account. In order to do so the amplitude must be related to the width along the x and y direction, and the angle of eccentricity. These parameters vary with wavelength and by the day of the experiment since the sample might be rotated slightly or the beam can aligned to a slightly off-axis. Both methods, gauss-fit and

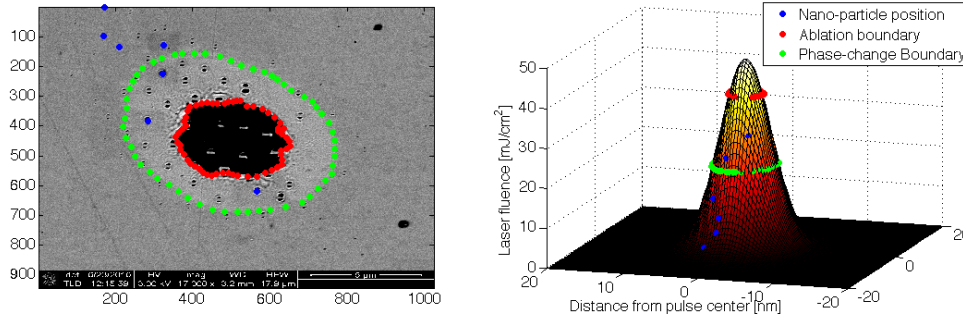


Figure 5.6: Shows the conversion from SEM image to a map of the laser fluence distribution in relation to the nano-particles. To the left a SEM image of the entire laser-spot is shown. The ablation and phase change boundary is marked with red and green points respectively while the nano-particles are marked with blue. To the right is the fit of a gaussian function to the two boundaries for which the fluence is corresponding to the threshold fluence values plotted in figure 5.3

pulse reproduction has been tried for data-analysis, and produce results that agree to an acceptable degree. The gauss-fitting method is however chosen for this thesis as it is most nimble and naturally gives a better agreement with phase change/ablation boundaries. The pulse reproduction method does however have the strong advantage of allowing for near-field mapping just below the phase change threshold. This gives a larger area exposed to a laser-fluence optimal for phase change by field enhancement. With the gauss-fit method this is not possible since two contour ellipses are needed for the fit and hence an ablation crater larger than or equal to the diffraction limited spot size must be present.

The gauss fitting results allows for fluence determination at a given set of coordinates with respect to the center of the laser-pulse. A number of nano-particles in different distances are chosen for close-up examination. Since the incoming fluence and threshold fluence is known the enhancement is found in areas with phase-change or ablation (depending on the fluence at the nano-particle). On a nano-scale SEM close up of the nano-particles the ablated or phase-changed areas are marked resulting in a contour plot of the near-field distribution. Since the contrast is binary (either ablation happens or it does not), the enhancement factor recorded is constant for a given nano-particle. The enhancement factor is determined as the ablation/phase-change threshold fluence divided by the local laser fluence at the position

of the nanoparticle,

$$Q_{Enh} = \frac{F_{Th}}{F_{NP}} \quad (5.8)$$

By examining several nano particles a contour plot with areas of different enhancement factors is made. An example of such a plot for 1350 nm laser light is seen in figure 5.7. Similar plots have been made for wavelengths spanning from 1250 nm to 1450 nm and will be analysed in the following section.

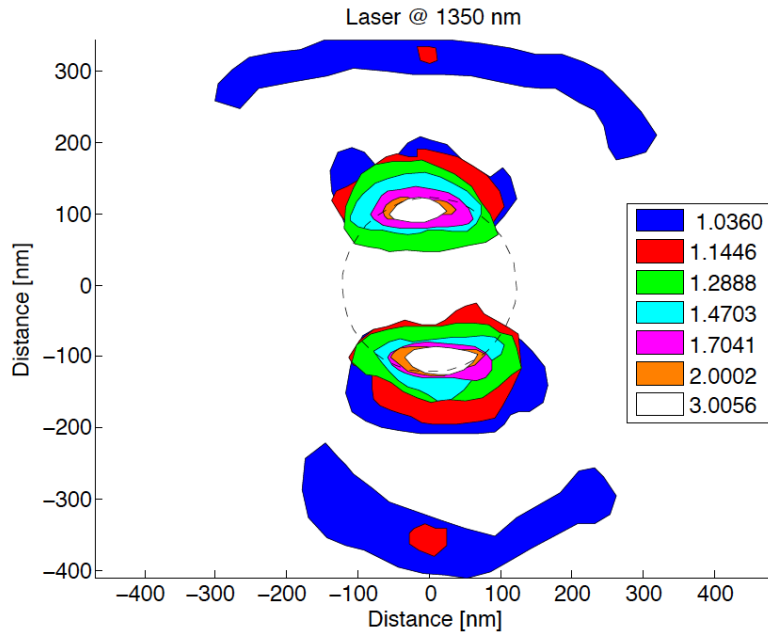


Figure 5.7: Shows contour plots of the near-field around gold nano-discs for a central laser wavelength of 1350 nm. The legend provides the enhancement factor  $Q_{Enh}$  for each zone.

---

## Results and discussion

### 6.1 Near-field contour maps

By the procedure described above the near-field enhancement is mapped out for several wavelengths. Since Silicon-based solar cells absorbs up to 1130 nm its the spectral region above this and up to the erbium absorption at 1560 nm that is of interest in the SunTune project. In figure 6.1 near-field contour maps is presented for wavelengths 1250, 1300, 1400 and 1450 along with the plot for 1350 nm in figure 5.7. Unfortunately the area with NP's deposited was filled, after the shots at the 5 wavelengths mentioned above, leaving no room for irradiations with 1500 nm and above. Since the EBL-system was down at the time no new experiments were made to widen the spectral region under investigation.

The contour plots in figures 5.7 and 6.1 has a few characteristics, valuable for correct interpretation. At sufficiently high laser fluence the nano-particle is expelled, due to the comprehensive amount of ablation. This means the areas with lowest enhancement factors and thereby closest to the laser ablation boundary, are an outline of the ablated area outside and underneath the nano-particle. For moderate energies the nano-particle remains on the GST and only the ablated areas outside the particles is mapped. The general LSP response are in the shape of a dipole as expected from the spherical case, however the field enhancement is very localized to the edges of the NP. As seen in 5.7 "wings" of near-field enhancement are present at 1350 nm. Since the wings are not seen for other wavelengths they are ignored for the comparative analysis. For wavelengths of 1350, 1400 and 1450 nm measurements are additionally done after removing the nanoparticles from the entire sample. This was done in a pursuit to resolve the phase change

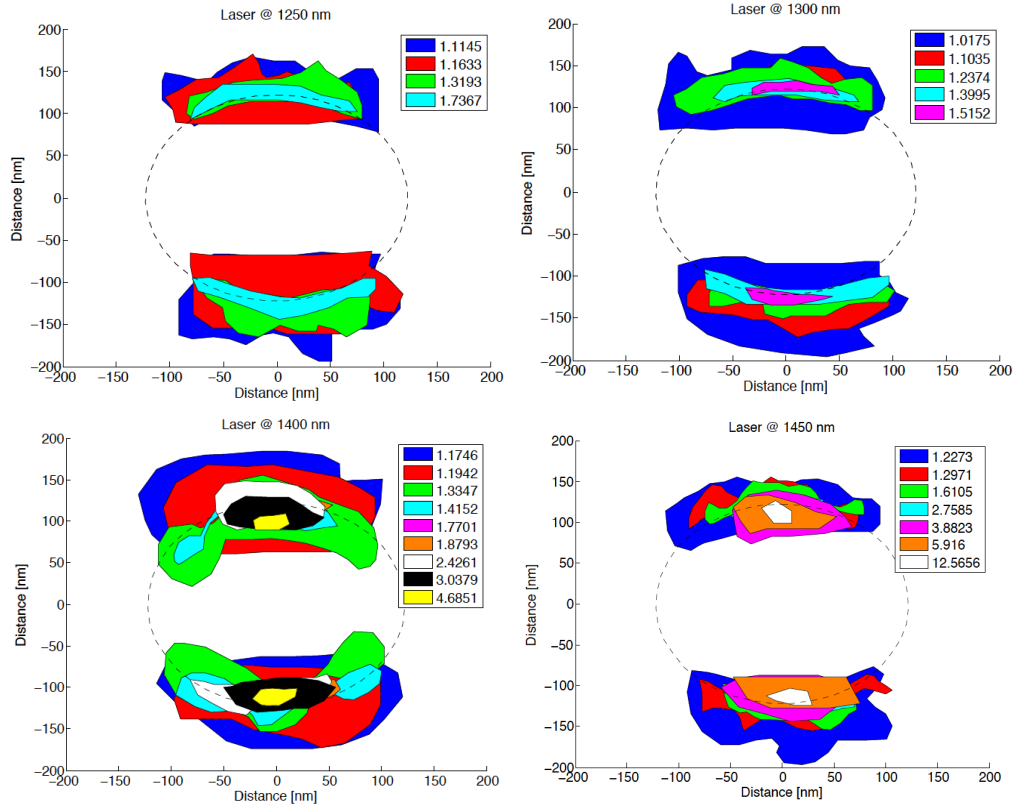


Figure 6.1: Shows contour plots of the near-field around gold nano-discs for laser wavelengths 1250 nm, 1300 nm, 1400 nm and 1450 nm. The legend provides the enhancement factor  $Q_{Enh}$  for each zone.

contrast near the particles. As discussed in section 5.2 no phase contrast is seen near the nano-particle even after removal. It did however reveal areas of higher enhancement (above 2) mainly underneath the nano-particle. It should be noted that these areas of higher enhancement were not present at 1250 and 1300 nm, even when observing post NP removal.

Due to the high number of free electrons in gold the NP's appear very bright on the SEM. This results in a glow around the NP, hiding ablated areas within approximately 10 nm distance of the NP-edge. An advantage gained from the NP's still being in place is that non-symmetric near-field distributions can be seen in relation to the exact position of the NP. An advantage of removing the NP is that it creates a more even ground for comparison as the NP's closest to the ablation boundary will be expelled anyway. Since NP's can only be removed from the entire sample measuring

the field enhancement with the NP's still present is in some cases required. Thus overall it is advantageous to map the field enhancement post removal of NP's for any quantitative analysis, although this practically requires destruction of the sample hindering further experiments on it.

## Resonance determination

A challenge regarding the results in figure 6.1 is quantitative comparison between wavelengths of the laser pulse. Enhancement factors are determined based on the position of each NP in relation to the pulse-center. This makes controlling and varying the exact enhancement factor practically impossible (at least with the spot size and NP density used here). The ablated region further differ significantly in size and shape. In order to use the area of the ablated region one has to restrict the measurements to being purely without nano-particles present. The method used for this thesis is measurement of the distance from the NP-rim to the furthest part of each ablated region at the axis of symmetry parallel to the E-field polarization. This method of measurement excels in the way that mappings with and without NP's present can be compared, but is heavily limited by the abnormalities in near-field pattern. A plot of the enhancement factor as a function of distance from the NP is seen in figure 6.2.

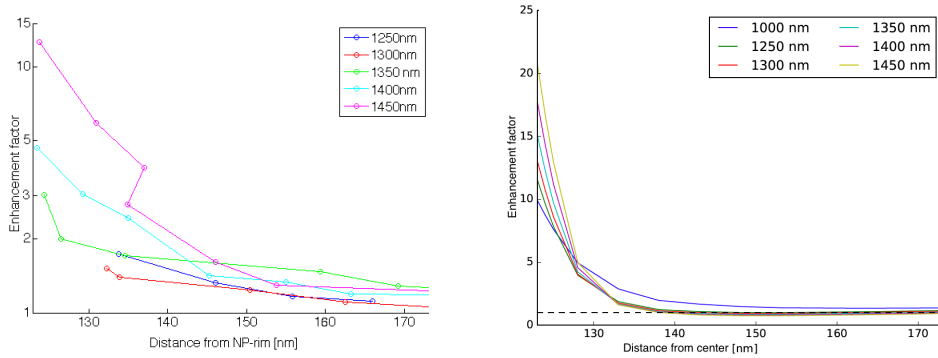


Figure 6.2: Shows the enhancement factor  $Q_{Enh}$  as a function of distance from the NP edge plotted for several laser wavelengths. The panel to the left shows the experimental data while the panel to the right originate from simulations. For the simulated data measurements of the field enhancement is recorded in 5 nm intervals of the distance to the NP centre. The y-scale of the experimental data is logarithmic for better distinction of the data at larger distances.

The interpretation of figure 6.2 is questionable. There is a tendency of asymptotic behaviour towards the edge of the NP. The resonance of the LSP seems to be at 1450 nm or above, however no completely convincing value of resonance can be determined from the data shown. For future work the resonance definition should be clearly defined since simulations reveal great difference in resonance for different methods of measure. This is also reflected in figure 6.2 where the lines cross making lower wavelength appear resonant for high distances.

Since the spectral width of the laser pulses is approximately 60 nm hardly any additional information is obtained by varying the laser wavelength in smaller steps. Near-field mapping from 1500 nm and upward in laser wavelength would give a more complete description. Another source of inconsistencies is the fundamental process of ablation. Ablation happens as a combination of single particle and cluster ejections from the surface. Combined with cracks in the GST and contaminations on the sample leads to a distorted ablated region on the nm scale. In addition the entire ablation boundary lights up both due to swelling at the rim and due to the slope down the crater. This makes defining the position of the ablation boundary difficult. This problem should be greatly minimized for phase-change mapping as discussed in the section below.

## Comparison with simulations

The deposition, laser irradiation and finally imaging makes the experimental determination of LSP resonance very time consuming and thereby badly suited for size and shape variation studies. The process of finding the right geometry is performed much faster and more nimble by Finite Element Method (FEM) simulation or ultimately through optimization. For the simulations to become a reliable tool there must be a convincing correspondence between the simulated LSP response and the actual near-field distribution. The results of a FEM simulation performed at 1350 nm for a nano-disc structure with dimensions matching the single gold discs described above is shown in 6.3.

The immediate observation is the absence of the "wings" seen in figure 5.7. Although a weak effect it has been observed not only at 1350 nm and the absence is a clear sign of discrepancy between the simulations and the measured near field. The source of the difference could be the particle geometry used in the simulations. So far the simulations are based upon a perfect cylinder, thereby not taking the characteristic truncation and rounding of edges from EBL-fabrication into account. A study of LSP response from a gold nano disc surrounded by a gold ring show large consequences from

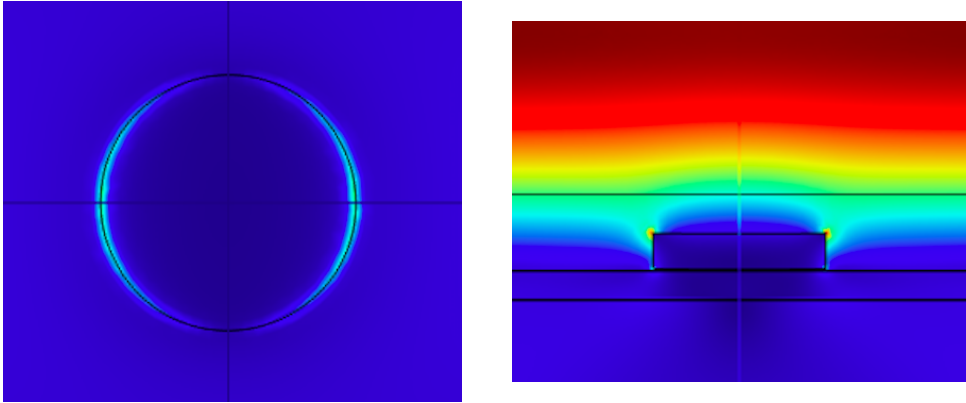


Figure 6.3: Shows the simulated LSP response at 1350 nm. The left panel corresponds to the plots in figures 5.7 and 6.1 only with horizontal polarization. The right panel shows the incident wave and gives insight to the distribution along the height of the NP.

the rounding of edges[61]. A shift in resonance frequency of  $\sim 300$  nm is reported although the effect is most likely more pronounced in the case of these coupled plasmon structures. According to the same study the rounding of edges does not introduce significant changes to the shape of the near field. Another source of the discrepancy could be interference or coupling of the LSP's. Initial simulations with neighbouring particles included show no sign of near field enhancement apart from the dipole response near the NP, however, the random distribution makes a rigid investigation difficult.

From the cross-section in the right panel of figure 6.3 it is clear that the field enhancement is by far strongest and most far-reaching in the air surrounding the particle and not in the underlying layer as desired. Apart from this immediate challenge it is clear that the height of recording the field strength is crucial. For the results in figure 6.2 and 6.3 the field enhancement is recorded at the boundary between air and GST. The simulations reveal that the field strength falls off very rapidly just a few nm's into the GST. This may have consequences on the material response since the excitation happen faster than the GST can thermalize. The outcome could be a mixed material response with ablation of the top part of the GST while the lower parts are switched to a-GST.

## 6.2 Coupled field enhancement

Advancing from single nano-discs to an ordered array of nano-disc pairs introduces three characteristic lengths to the resonance criterion; the gap between the NP-pair and the distance between pairs parallel and perpendicular to the pair-axis. The ordering further introduces a strong dependency on polarization. Investigations of similar LSP geometries report that there could be a significant enhancement in the gap between the two discs constituting each NP-pair[62]. However this effect has not been studied yet, since the gap varies across the sample and the NP's complicate the measurement in this tight gap. The coupling between the nano-particles further seems to dampen the near-field enhancement in the vicinity of the particle. With a steady gap and a sample ready for particle removal the in-gap enhancement could be analysed, for now the focus is on the enhancement in the region between the NP-pairs. The significantly larger enhanced regions that in addition lies in between the NP-pairs, allows measurement without obstructions from the NP. In the analysis of the coupled near-field enhancements near-field effects in the immediate vicinity of the particles is consequently ignored. As expected based on experience from single particles and the possible heat reservoir explanation the enhancement "far" from the NP's allow for GST phase shifting to be recorded. The near-field can thereby be mapped out using both phase-change and ablation as a measure of local fluence.

### Ablation vs. Phase change for local fluence detection

Since phase change and ablation are used in the exact same way for the near-field mapping a comparison of the two is in place. In figure 6.4 contour plots are made from NP's around the same laser spot (1450 nm irradiation polarized along the pair-axis) with respectively ablation (left) and phase change (right).

From figure 6.4 it is clear that the near-field can indeed be mapped by both ablation and phase change with the current setup and imaging capabilities. The fact that the wings above and below the particle are more pronounced in the bottom is due to the fact that this side was oriented towards the pulse-centre. This is a clear sign that the assumption of a constant local field at the nano-particle is too simple for a detailed analysis of larger areas. To minimize the error from this only particles at a small angle above or below the pulse centre is used for contour-plots, giving distortion only in one direction. The near-field distribution does however change in shape and resolvable features beyond the expected disagreement when comparing

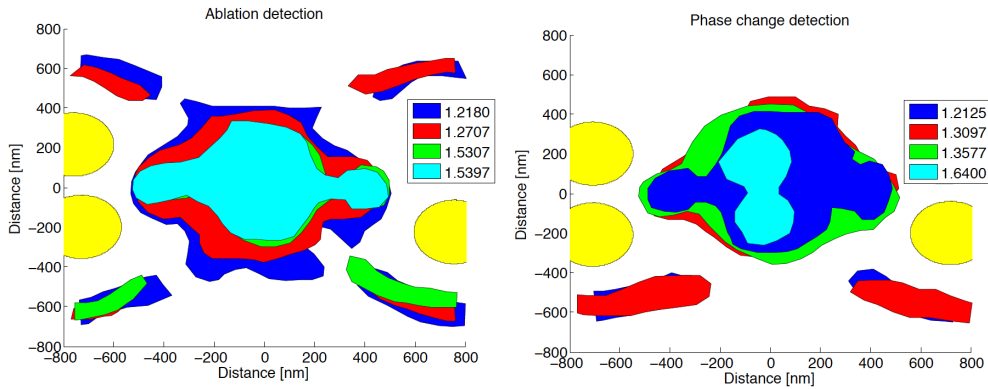


Figure 6.4: Shows a contour plot of the near-field distribution in the region between two pairs of nanoparticles. The incident laser pulse has a central wavelength of 1450 nm and is polarized along the axis connecting the NP-pair. On the left figure the near-field is mapped by detecting areas with ablation whereas the image on the right the detection of phase change is performed. Notice that a NP is hidden underneath the legend on both figures.

ablation to phase change. For ablation the rather precise overlap of the two regions of  $\sim 1.53$  times enhancement indicate that the shapes are reliable. For sufficiently low enhancements mapped by phase change the affected region becomes so extensive that its doubtful whether the border is determined by field strength or by the heat reservoir effect of recrystallization near the nano-particles. In addition the blue area of lowest enhancement mapped by phase change is considerably smaller than the two cases with slightly lower incoming intensity. No explanation besides poor detection of phase shift boundaries has been found for this discrepancy. Measurements where done at 1450 nm since this frequency showed an intensive LSP response. The area of field enhancement could however be are more indirect consequence of the nano-particles coupling to a create a dark PHM mode. This would change the interpretation of the area in between creating some regions where a better coupling does not correspond to a larger ablated area. No clear conclusion regarding this interpretation is given based on the data obtained so far. The NP-pair configuration is thus used purely for assessment of phase-change versus ablation for near-field mapping as well as an analysis based on the plasmon hybridization model in the following section.

With the detail of resolvability obtainable so far, mapping near-field distributions with ablation seems like the best choice. Apart from better reso-

lution, ablation benefits from the fact that it can be done on basically any material. This removes the need of correcting the difference in refractive index between GST and the material on which the NP's are placed for their application. Mapping via phase-change on the other hand has the potential to become far superior if better control and imaging of the phase change is achieved. Reports has been made of 8-level phase contrast in optical transmission[22] for GST. If this is achieved on nm scale detailed info of the near-field distribution could be obtained from a single nano-particle. To accomplish better mapping from phase change the imaging of amorphous versus crystalline GST must be significantly improved. This could be achieved in SEM perhaps by another detector or at the better SEM equipment in the clean-room at the nano-department at Aarhus University. Phase contrast on SEM has been documented in [21] while [50] has promising results using conductive AFM. Both studies show a more convincing distinction between GST phases on nm scale.

### Hybridized plasmonic resonances

For the coupled plasmons, there is not enough experimental data to determine the resonance frequency as it was done for single particles. There is however observed a clear change in LSP response across the wavelengths included in the experiment. The position of the resonance is according to the plasmon hybridization model (PHM) shifted with respect to the resonance of a single particle. Since the NP constituting the array is larger than the single ones examined in section 6.1, the exact resonance is not known but is expected to lie above slightly 1450 nm.

Observation of the LSP response reveals that with polarization along the joint axis of the NP-pair the near-field has two different distributions. At 1400 nm and 1450 nm the entire region between two pairs is enhanced by the near-field whereas it for 1500 nm only amounts to two single spots between the two corresponding NP's from each pair. At 1570 the enhancement is almost exclusively at the position of the "wings" known from single particle resonances. Pictures of the LSP response to parallel polarized light at 1400 nm and 1570 nm is seen in figure 6.5.

With the laser polarization perpendicular to the joint axis of the NP-pair the strongest response is similarly found at 1400 nm and 1570 nm. They differ in the way that the near-field at 1400 nm has highly localized bright spots directly between two pairs and closer to the NP, whereas the near-field at 1570 is more distributed to the entire region between the NP-pairs, see figure 6.6. Referring back to section 2.2 the coupling between two dipoles

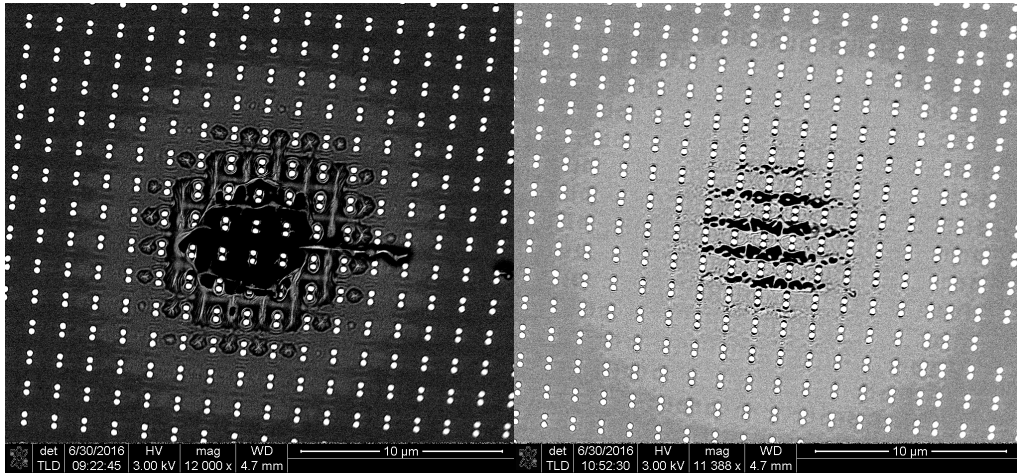


Figure 6.5: Shows an overview of the LSP response for 1400 nm (left panel) and 1570 nm (right panel) laser light taken with back-scattered electron on SEM. The light polarization is parallel to the axis connecting the NP-pair. The pulse energies were measured to be  $0.235 \mu\text{J}$  and  $0.310 \mu\text{J}$  for the two shots, but the difference in damage threshold should be kept in mind when comparing. The difference in brightness is purely due to different settings on the SEM.

can be either side by side (*sbs*) or end to end (*ete*) determined by the light polarization in relation to the particles joint axis. For light polarized along the joint axes of the two particles the dipoles align *ete* with two possible configurations. With the positively charged ends pointing towards each other the combined dipole moment is negligible due to mutual cancellation of the dipole moments, whereas two dipoles pointing in the same direction results in a large dipole. The two orientations are referred to as dark and bright plasmon modes since the bright mode couples effectively with the plane wave of an incoming light field. The resonance is shifted according to the phase-match between the dipoles. For the bright *ete* mode the dipoles are in phase and the frequency is lowered giving a red-shift in plasmon resonance. This agrees with the observation of a LSP resonance at 1570 nm or above. Accordingly the dark mode is blue-shifted. For the *sbs* alignment the bright mode results in dipoles out of phase, and hence blue-shifted. This corresponds to the observation that the LSP resonance with perpendicular orientation is at 1400 nm or lower.

For both polarizations LSP response is seen in areas where the simple PHM model predicts dark states or simply poor resonance. This hints that the

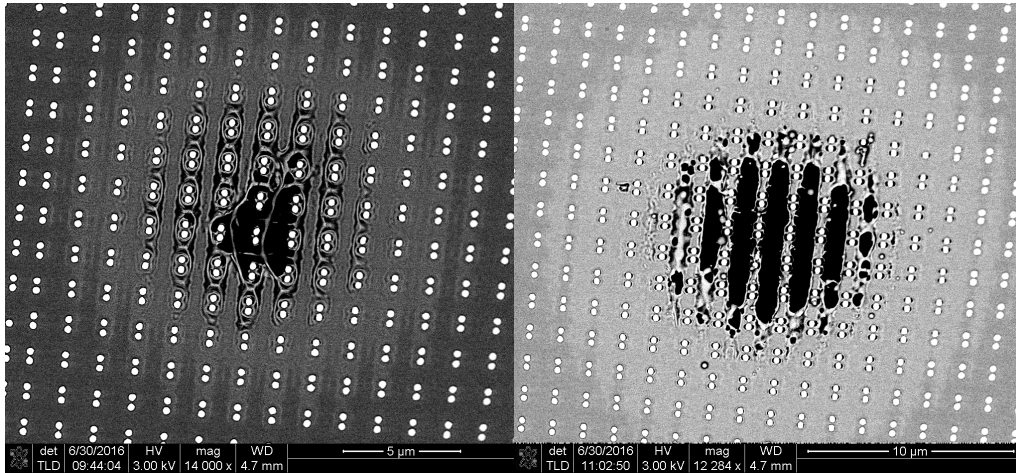


Figure 6.6: Shows an overview of the LSP response for 1400 nm (left panel) and 1570 nm (right panel) laser light taken with back-scattered electron on SEM. The light polarization is perpendicular to the axis connecting the NP-pair. The pulse energies were measured to be  $0.190 \mu\text{J}$  and  $0.391 \mu\text{J}$  for the two shots, but the difference in damage threshold should be kept in mind when comparing. The difference in brightness is purely due to different settings on the SEM.

PHM description using solely excitations of low order ( $l = 1$ ), does not provide the full description of plasmonic effects happening. A more thorough investigation is needed in order to give any qualified explanation, so the possible explanation will just be briefly discussed. First of all it has been found that dark modes can be excited by highly focused laser beams[11], which is the case in these experiments. Since the modes will be dark regardless of the ability to excite them this might lead to a field where the dipole moments cancel out at regions of typical high enhancement. This would correspond to having a local reduction rather than enhancement of the incoming field and might be the case observed for instance at 1400 nm for the *ete*-alignment. Here the region above and below the NP-pairs is almost completely unaltered while the surrounding area is ablated.

Another possibility is excitation of higher order plasmonic modes. As mentioned in section 2.2 the spatial distribution of the plasmon modes resemble that of the atomic orbital, at least for spherical particles. Assuming some similarity with this picture for nano-discs the higher order modes would introduce multi-poles with a more nuanced distinction of bright/dark modes. Along with higher order modes symmetry is additionally introduced on a

larger scale. Considering each NP-pair as a unit, *ete* and *sbs* coupling is present simultaneously but for slightly different frequencies. The possibility of multiple excited plasmons at once introduces interference to the resonance criterion, resulting in fano-resonances, briefly explained in section 2.2. The complete response is quite complicated with this mixture of hybridization and fano resonance. However, since the fano resonance is as narrow spectrally as the most narrow LSP resonance constituting the interference there is hope that detection of fano-resonances could help resolve the different LSP-modes. This spectral analysis would be performed much more efficiently by e.g. absorption spectroscopy. With more information on the resonances at play hopefully more information can be extracted from the near-field mappings.

---

## Outlook

### 7.1 SunTune

My departure from this project is in many ways at the most interesting time imaginable. Through the last few months massive advancement has been made leading up to a point where quantitative two-dimensional mapping of the near-field is possible on nm scale. So far the experiments have been conducted on rather randomly chosen structures not necessarily well suited for field enhancement. With the numerical simulations also advancing quickly the scene is set for more though through near-field investigations. By careful design nano particles can be made resonant with the 1500 nm wavelength needed in the erbium up-conversion. Furthermore enhancement factors for the particles studied so far has mainly been in the 1-2.5 regime. Even with this minimal enhancement factor rather detailed near-field distributions has been mapped. For nano-particles producing enhancement factors of 10, 20 or even higher the resolution would see massive improvement. An example of a NP shape that resonates at "SunTune wavelengths" is given in [61]. With gold rings surrounding smaller gold discs a LSP resonance at 1530 nm is achieved. The field enhancement is by numerical simulations found to reach 20 times the incoming field at various locations in and around the NP.

The end-goal for the SunTune project regarding LSP enhancement is to determine the optimum shape and distribution of nanoparticles. This is done by topological optimization as quickly introduces in section 2.2. The measurement of future optimized nanoparticles does however introduce a number of challenges.

The challenge of most fundamental character arises from the desire to map out the near-field in the third dimension. For this to be realized the method of mapping the near-field must be changed, maybe completely abandoning GST as imaging host. The third dimension could be achieved by introducing a buffer layer transparent to the infrared region. Since the sputtering of thin films can be controlled at nm thickness this would allow for a step-wise mapping of the near-field distribution down into the sample. The introduction of a buffer (e.g. quartz) would however shift the LSP resonance as this is quite sensible to the refractive index of the surrounding environment. The use of a buffer is challenged by the ultra-short pulses since strong-field ionization will eventually lead to breakdown of any dielectric, spoiling the transparency. Another way to obtain 3D near-field mapping could be utilizing two photon polymerization, an effect already used for sub- $\mu\text{m}$  3D printing. Due to the widespread use in 3D printing extensive research and development has been made on the gel used as imaging host. The diffraction limit naturally means that the consequences of going to nm scale is unknown for the photosensitive gels. Whereas the introduction of a buffer layer would benefit from the knowledge attained in this thesis the two photon polymerization method would require new characterization work and to some extent a new experimental set-up. A disadvantage of the buffer-layer strategy is the stepwise investigation of the third dimension which is immensely consuming.

Once the optimized nanoparticles have been designed, fabricated and characterized the assembly of a solar-cell capable of harvesting a wider spectrum can begin. In order to ensure that this crucial step of assembly succeeds, parts of the SunTune project is already now working on investigations of consequences from assembly. This includes studies of life-time changes of the erbium ions when situated close to the gold NP's as well as changes in LSP resonance due to optical parameters of the multilayer device. For the assembly a comprehensive theoretical knowledge on the LSP response is needed as well. In conclusion there is still plenty of work to be done in the SunTune project regarding mapping and describing the near-field effects of LSP's. With this thesis an experimental platform that can aid in this work has been build, presented and characterized.

## 7.2 General usage

The work presented in this thesis has applications reaching far beyond solar cells and the SunTune project. This is reflected in the enormous expansion

of plasmonic founded articles over the last 15 years in scientific journals covering physics, engineering, chemistry, biology, medicine and more. In nearly every study examining LSP resonances (e.g. [17],[61], [62] and [63]), the procedure is to experimentally determine the NP shape by SEM or AFM as well as the resonance wavelength through absorption spectroscopy measurements. All details of the enhancement factor and spatial distribution of the near-field is based on simulation. Near-field mapping is an absolutely critical bridging tool between the simulations and a reality full of imperfections and side-effect not included in the computing algorithm. The method presented in this thesis meets many of the requirements to a robust and precise depiction of the enhancement both in shape and strength. This could lead to increased LSP-optimization towards numerous applications.

One field of plasmonic research aims to resolve the quantum mechanical energy solutions to molecular bonding. This is done via plasmons by forming plasmonic molecules, which are plasmonic structures arranged in relation to each other to resemble a molecule[20]. Mapping of energy diagrams of molecules through plasmons, has been performed from the spectral position of the resonance [62]. With the advances in numerical simulations and experimental mapping of the near-field, the next step in this research could be a spatial investigation of the electronic distribution in molecules. The discussions from above about taking plasmonic near-field mapping to three dimensions is highly relevant in the molecular imitations as-well, since this would allow to expand the field beyond planar molecules.

Another more practical application of LSP resonances is in the rapidly expanding field of integrated photonics. Since electronics are on many fronts hindered from further improvement of data-transmission rates and computational power the change to optically based systems is starting to happen. For this sub  $\mu m$  light manipulation is central and plasmons could thus very well play a vital role in the transition to optical circuits. Proposed utilizations include spacial splitting of wavelength [20], nano-scale antennas [64] and nano-lithography [65].

---

## Conclusion

The near-field arising from localized surface plasmon resonances has in this thesis been mapped experimentally. In order to do this an experimental platform has been developed. This platform is capable of irradiating samples at micrometer precision while measuring the pulse energy of individual 35 femtosecond laser pulses. In order to attain information of the near-field the metal particles are placed on a phase changing thin film of the material  $Ge_2Sb_2Te_5$  (GST). For laser irradiation above a certain threshold intensity the GST can switch from crystalline to amorphous ordering while for even higher intensities the material is ablated. Both processes provide binary contrast of the field intensity at the position of investigation.

The excitation of GST by ultra short laser-pulses has been experimentally investigated providing optical parameters allowing for simulations as well as calculations of threshold fluence for material alteration. The threshold fluences were found to vary significantly with wavelength in the region of 1300 nm to 1570 nm laser radiation. In order to detect the regions of GST exposed to fluence above threshold, the imaging of both ablation and phase-change of GST at nanometer scale (well below the diffraction limit!) has been investigated. Whereas ablation is easily detected, phase-change proves to be more challenging since the main material change is in the optical reflectivity. A clear phase-distinction is achieved using backscattered electrons in SEM however the task of achieving phase contrast is still a working progress.

For single gold-discs the near-field is mapped, providing a quantitative measure of the 2D near-field distribution at the surface of the GST. Comparison of the near-field across different wavelengths lead to a determination of the

LSP-resonance at 1450 nm (or above) for gold-discs with a diameter of 245 nm and a height of 50 nm. Areas with local fields up to 12 times higher than the incoming field is observed. The shape of the LSP-responce is found to resemble a dipole as expected from theory, however an additional region further from the nano-particle is seen to be enhanced as-well (See figure 5.7). This effect is not observed in the computer simulations and is clear evidence of the value of this thesis. To obtain reliable simulations, experimental comparison is crucial. Based on observations of the phase-change near the NP it is clear that the area within  $\sim 100$  nm from the particle edge is not switched in phase. A theory of this observation is explained and assessed in section 5.2. Regardless of the origins of this absence of phase shift it poses a challenge towards mapping near fields in the immediate vicinity of metal particles with the method used in this thesis.

For pairs of gold-discs arranged in an array both coupled plasmon modes and interference between plasmon modes must be included in the LSP-response. The observed near-field patterns are discussed in relation to the plasmon hybridization model, where a good qualitative agreement is found. In addition an assessment of the pros and cons in detecting near-field distributions with ablation versus phase change is given. For the time being ablation gives the most accurate near-field imprints, however the future potential is grater for phase change near-field detection.

The thesis finally outlines future challenges in the mapping of optical near-fields arising from localized surface plasmon resonances. This is done both in relation to the SunTune project and in a broader scope of general applications.

---

## Dansk resume

*Dette resume er tiltænkt lægmænd og er således en kvalitativ forklaring af arbejdet beskrevet i dette speciale. Målet er at motivere arbejdet samt forklare hvordan det principielt er udført. Desuden klargøres det hvad arbejdet i dette speciale kan bruges til i den virkelige verden.*

Dette speciale er afleveret som afsluttende opgave på kandidat uddannelsen i fysik på Aarhus Universitet. Specialet er udført over det sidste år som en del af det større forskningsprojekt SunTune, hvis formål er at forbedre effektiviteten af solceller. Solcelle markedet er domineret af silicium baserede paneler, da silicium er en halvleder som kan absorbere lys fra hele det synlige område og et stykke ind i det infrarøde. Lys kan kvantiseres i fotoner (lys partikler) og energien af disse fotoner afhænger af bølgelængden, og dermed farven af lyset. Fælles for alle silicium solceller er at de ikke kan udnytte de lavenergetiske fotoner (infrarøde) da disse ikke kan eksitere elektroner på tværs af båndgabets i silicium og dermed ikke bidrager til strømproduktionen. Af det lys der når jorden befinder 19 % sig i dette energi område og der er derfor en stor potentiel gevinst ved at op-konvertere lyset til lys med lavere bølgelængder og dermed højere energi (se figur 1.2 og 1.3). Denne op-konvertering forløber som en to-foton proces i erbium ioner og kræver således høj intensitet for at forløbe effektivt, hvorfor sollyset skal fokuseres for at opnå stor effekt af konverteringen. Fokusering af lyset kan udføres med metalpartikler på nanometer størrelse grundet plasmoniske effekter.

Plasmoniske effekter opstår ved at det indkommende lys inducerer oscillation af de frie elektroner i metal partiklerne (se figur 2.2). Da partiklerne

er mindre end lysets bølgelængde er betingelserne for resonans ekstremt følsomme overfor størrelse, form og indbyrdes placering af metal partiklerne. Ved omhyggeligt design af metalpartikler kan man således skabe forstærkning af det elektriske felt med kontrol over både feltfordelingen og resonans bølgelængden. Forstærkningen sker dog på en skala sammenlignelig med bølgelængden, kaldet nærfeltet. Dette besværliggør kortlægningen af det elektriske felt eftersom opløsning på nanometer skala ikke kan opnås med konventionelle detektions metoder. Dette projekt har til formål at måle den rumlige udbredelse af nærfelts forstærkning omkring nanopartikler. Dette gøres ved hjælp af en kort-puls laser og materialet GST. GST har som egenskab at skifte fase fra krystalin til amorf ved bestråling fra en ultrakort laser puls (se figur 2.6). Da der er forskel i den optiske refleksivitet kan denne fase ændring efterfølgende detekteres eksempelvis i et elektron mikroskop som kan opløse detaljer ned på nm skala. Eftersom faseskiftet i GST sker ved en bestemt energitæthed kan skiftet bruges som en binær kontrast for styrken af feltet der rammer materialet. Det samme gælder for ablation, som er processen hvor materiale smeltes og fordampes af laserpulsens efterladende et krater. En vigtig del af dette projekt har været bestemmelse af tærskel fluenser for ablation og faseskift ved bølgelængder mellem 1300 og 1600 nm. Det viser sig at disse værdier er meget afhængige af bølgelængden i dette område hvor tærskel fluensen fordobles over intervallet (se figur 5.3). Dette eksperimentelle arbejde samt de efterfølgende nærfelts undersøgelser er udført på en eksperimentel opstilling opbygget undervejs i projektet.

Ablation og faseskift af GST bruges til at opmåle nærfeltet omkring nanopartikler bestrålet med laserlys. Ved at observere materiale ændringer omkring nanopartikler under varierende bestrålings-energi kan nærfelts forstærkningen kortlægges. Dette fører til afbildninger af nærfeltets rumlige fordeling som kan ses i figur 5.7, 6.1 og 6.4. For guld diske med en diameter på 245 nm og en højde på 50 nm bestemmes resonansen samt forstærkningen. Resonansen bestemmes til 1450 nm og forstærkninger på over 10 gange det indkommende felt observeres. Computer simuleringer viser lignende resultater for resonansen, men giver ikke helt samme fordeling af nærfeltet (Se figur 6.3).

For guld diske placeret to og to i par fordelt i et regelmæssigt gitter introduceres yderligere en kobling mellem flere plasmon resonanser. Denne kobling fører til en øget forstærkning der er afhængig af polarisationen af laser-lyset i forhold til gitteret. Konfigurationen med par af nanopartikler analyseres ud fra plasmon hybrid modellen, som ud fra betragtninger om kobling af dipoler kan forudsige skift i resonansfrekvens. Med både par-

tikel geometri og den indbyrdes placering som frie parametre kan nærfelts fordelinger og disses resonans fintunes. Eksperimentel bekræftelse af de simulerede plasmoniske effekter er en vigtig milepæl i vejen mod fuldt kontrollerbare plasmoniske forstærkninger. Metoden som er fremlagt i dette speciale skal udvikles yderligere for at kunne tilfredsstille krav om eksempelvis tredimensionel nærfelts kortlægning.

Anvendelses mulighederne for plasmoner er mange. For dette projekt ligger fokus på solceller hvor plasmoner er en vigtig brik i en potentiel effektivitets forøgelse på 4 procentpoint. Denne forøgelse skal ses i forhold til en nuværende effektivitet på 25 % samt det faktum at aktivering af det infrarøde område vil udvide solcellens potentiale i overskyet vejr og tidspunkter hvor solen står lavt, eftersom det infrarøde lys har stærkere penetration end det synlige lys i disse situationer. Andre anvendelses områder er bølgelængde følsomme lysensorer, grundforskning om energi niveauer i molekyler og materialebehandling på nanometer skala. Plasmoner åbner generelt set muligheder for at manipulere lys ned på en præcision mere end 10 gange bedre end det ellers fundamentalt tillades af diffraktions grænsen i konventionel optik (med normale linser kan synligt lys aldrig fokuseres under  $\sim 200$  nm).

---

## Bibliography

- [1] Harry A Atwater. “The promise of plasmonics.” In: *Scientific American* 296.4 (2007), pp. 56–63.
- [2] Peter Würfel. *Physics of Solar Cells*. 2. ed. Wiley-VCH, 2009.
- [3] Donald A. Neamen. *Semiconductor Physics and Devices*. 4th ed. McGraw-Hill, 2011.
- [4] A. De Vos and H. Pauwels. “On the Thermodynamic Limit of Photovoltaic Energy Conversion”. In: *Applied Physics* 25 (1981), pp. 119–115.
- [5] Octavi Semonin et al. “Multiple exciton generation in a quantum dot solar cell”. In: *Spie* (2012), pp. 1–3.
- [6] William Shockley and Hans J. Queisser. “Detailed Balance Limit of Efficiency of p-n Junction Solar Cells”. In: *Journal of Applied Physics* 32.3 (1961), p. 510.
- [7] Martin A. Green et al. “Solar cell efficiency tables (Version 47)”. In: *Progress in Photovoltaics: Research and Applications* 24 (2015), pp. 3–11. URL: <http://dx.doi.org/10.1002/pip.1160>.
- [8] E Lifshitz et al. “Air-Stable PbSe / PbS and PbSe / PbSe<sub>x</sub>S<sub>1-x</sub> Core - Shell Nanocrystal Quantum Dots and Their Applications”. In: *Journal of Physical Chemistry* 110 (2006), pp. 25356–25365.
- [9] Suntune Steering Committee. “High-efficiency solar cells by spectral transformation using nano- optical enhancement ( SunTune )”. In: Dep. of Physics, iNano, Engineering and external partners. Aarhus, 2015.

- [10] Sabrina Rostgaard Johannsen. “Upconversion of near-infrared light through Er doped TiO<sub>2</sub>, and the effects of plasmonics and co-doping with Yb”. PhD thesis. University of Aarhus, 2015.
- [11] Matthew Pelton and Garnett W. Bryant. *Introduction to Metal-Nanoparticle Plasmonics*. 1st. ed. Wiley, 2013.
- [12] Peter Balling. “Ultrashort-pulse excitation of materials”. Doctor Dissertation. Aarhus University, 2014.
- [13] J Siegel et al. “Rewritable phase-change optical recording in Ge<sub>2</sub>Sb<sub>2</sub>Te<sub>5</sub> films induced by picosecond laser pulses”. In: *Applied Physics Letters* 84.13 (2004), pp. 2250–2252.
- [14] Stefan A Maier. *Plasmonics: Fundamentals and Applications*. 1st ed. Springer, 2007.
- [15] Neil W Ashcroft and David N Mermin. *Solid State Physics*. 1st ed. Brooks Cole, 1976.
- [16] Philip Hofmann. *Surface Physics, an introduction*. 1st, ed. 2013.
- [17] C H Chou and F C Chen. “Plasmonic nanostructures for light trapping in organic photovoltaic devices”. In: *Nanoscale* 6 (2014), pp. 8444–8458.
- [18] Craig F Bohren and Donald R Huffman. *Absorption and Scattering of Light by Small Particles.pdf*. 1. ed. New York: Wiley, 1983.
- [19] J J Mock et al. “Shape effects in plasmon resonance of individual colloidal silver nanoparticles”. In: *Journal of Chemical Physics* 116.15 (2002), pp. 6755–6759.
- [20] Nir Zohar et al. “The Simplest Plasmonic Molecules : Metal Nanoparticle Dimers and Trimers”. In: *Journal of Photochemistry and Photobiology C: Photochemistry Reviews* 21.October (2014).
- [21] Christin David et al. “Near-field nanoimprinting using colloidal monolayers”. In: *Optics Express* 22.7 (2014), pp. 8226–8233.
- [22] Carlos Rí et al. “Integrated all-photonic non-volatile multi-level memory”. In: *Nature Photonics* 9.September (2015), pp. 725–732.
- [23] Agostino Pirovano et al. “Electronic Switching in Phase-Change Memories”. In: *IEEE TRANSACTIONS ON ELECTRON DEVICES* 51.3 (2004), pp. 452–459.
- [24] Kostiantyn Shportko et al. “Resonant bonding in crystalline phase-change materials”. In: *Nature Materials* 7.August (2008).

- [25] Lutz Waldecker et al. “Time-domain separation of optical properties from structural transitions in resonantly bonded materials”. In: *Nature Materials* 14.October (2015), pp. 991–996.
- [26] J Robertson et al. “Electronic and atomic structure of Ge<sub>2</sub>Sb<sub>2</sub>Te<sub>5</sub> phase change memory material”. In: *ScienceDirect: Thin Solid Films* 515 (2007), pp. 7538–7541.
- [27] B Huang and J Robertson. “Bonding origin of optical contrast in phase-change memory materials”. In: *PHYSICAL REVIEW B* 81 (2010), pp. 1–4.
- [28] S I Anisimov et al. “Electron emission from metal surfaces exposed to ultrashort laser pulses”. In: *Soviet Physics JETP-USSR* 39 (1974), pp. 375–377.
- [29] Peter Balling and J Schou. “Femtosecond-laser ablation dynamics of dielectrics: basics and applications for thin films.” In: *Reports on progress in physics. Physical Society (Great Britain)* 76.3 (2013), p. 036502.
- [30] Bärbel Rethfeld et al. “Modelling Ultrafast Laser Ablation”. In: *Journal of Physics: Applied Physics* (2016).
- [31] M. J. Shu et al. “Ultrafast sub-threshold photo-induced response in crystalline and amorphous GeSbTe thin films”. In: *Applied Physics Letters* 102.20 (2013), pp. 201903–201903–4.
- [32] J Siegel et al. “Amorphization dynamics of Ge<sub>2</sub>Sb<sub>2</sub>Te<sub>5</sub> films upon nano- and femtosecond laser pulse irradiation”. In: *Journal of Applied Physics* 103 (2008).
- [33] Kirill V Mitrofanov et al. “Sub-nanometre resolution of atomic motion during electronic excitation in phase-change materials”. In: *Nature Scientific Reports* 6.October 2015 (2016), pp. 1–9.
- [34] J Kalikka et al. “Nucleus-driven crystallization of amorphous Ge<sub>2</sub>Sb<sub>2</sub>Te<sub>5</sub>: A density functional study”. In: *PHYSICAL REVIEW B* 86 (2012).
- [35] D. Loke et al. “Breaking the Speed Limits of Phase Change Materials”. In: *Science* 336.June (2012), pp. 1566–1569.
- [36] V Weidenhof et al. “Atomic force microscopy study of laser induced phase transitions in Ge<sub>2</sub>Sb<sub>2</sub>Te<sub>5</sub> Atomic force microscopy study of laser induced phase transitions”. In: *Journal of Applied Physics* 86.10 (1999).
- [37] Peter W Milonni and Joseph H Eberly. *Laser Physics*. New Jersey: Wiley, 2010.

- [38] YanYing Zhao et al. “Generation of 7-fs laser pulse directly from a compact Ti:sapphire laser with chirped mirrors”. In: *Physics, Mechanics and Astronomy: Science in China Series G* 50.3 (2007), pp. 261–266.
- [39] D H Sutter et al. “Semiconductor saturable-absorber mirror assisted Kerr-lens mode-locked Ti:sapphire laser producing pulses in the two-cycle regime.” In: *Optics letters* 24.9 (1999), pp. 631–3.
- [40] RP Photonics. *Fourier Transform Limit*. 2016. URL: [https://www.rp-photonics.com/transform{\\\_}limit.html](https://www.rp-photonics.com/transform{\_}limit.html) (visited on 05/17/2016).
- [41] Spectra-Physics. “Mai Tai SP–manual”. In: (2010).
- [42] Spectra-Physics. *Solstice User Manual*. 2010.
- [43] F Pedrotti and L Pedrotti. *Introduction to Optics*. 2. ed. Prentice-Hall, 1993.
- [44] Sebastian Uhlig. “Generation of White Light Supercontinuum”. In: *Self-Organized Surface Structures with Ultrafast White-Light*. 1 st. Springer, 2015. Chap. 2, pp. 12–18.
- [45] Bahaa E. A. Saleh and Malvin Carl Teich. “Nonlinear Optics”. In: *Fundamentals of Photonics*. 2nd. John Wiley & Sons, 2007. Chap. Ch. 21, pp. 873–927.
- [46] Robert W. Boyd. *Nonlinear Optics*. 3rd ed. Academic Press, 2008.
- [47] Australian Microscopy and Microscopist Research Facility. *SEM infopage*. 2016. URL: <http://ammrf.org.au/myscope/sem/introduction/> (visited on 07/13/2016).
- [48] A Bogner et al. “A history of scanning electron microscopy developments : Towards “ wet-STEM ” imaging”. In: *ScienceDirect: Micron* 38 (2007), pp. 390–401.
- [49] K. D. Vernon-Parry. “Scanning Electron Microscopy : an introduction”. In: *IEEE TRANSACTIONS ON ELECTRON DEVICES* 13.4 (2000), pp. 40–44.
- [50] Fei Yang et al. “Nanoscale multilevel switching in Ge<sub>2</sub>Sb<sub>2</sub>Te<sub>5</sub> thin film with conductive atomic force microscopy”. In: *Nanotechnology* 27 (2015).
- [51] Young Soo Song and Chee Won Chung. *Characteristics of Ge<sub>2</sub>Sb<sub>2</sub>Te<sub>5</sub> Thin Films Deposited by DC Magnetron Sputtering*. 2003.
- [52] Ki-bum Kim. “Investigation of the optical and electronic properties of GeSbTe phase change material in its amorphous , cubic , and hexagonal phases”. In: *Journal of Applied Physics* 97.April (2005).

- [53] Jeppe Byskov-Nielsen et al. “Ultra-short pulse laser ablation of metals: Threshold fluence, incubation coefficient and ablation rates”. In: *Applied Physics A: Materials Science and Processing* 101.1 (2010), pp. 97–101.
- [54] Ke Zhang et al. “Different crystallization processes of as-deposited amorphous Ge<sub>2</sub>Sb<sub>2</sub>Te<sub>5</sub> films on nano- and picosecond single laser pulse irradiation”. In: *Physica B* 407.June 2016 (2012), pp. 2447–2450.
- [55] Y. Liu et al. “Crystallization of Ge<sub>2</sub>Sb<sub>2</sub>Te<sub>5</sub> films by amplified femtosecond optical pulses”. In: *Journal of Applied Physics* 112.12 (2012), p. 123526.
- [56] V Weidenhof et al. “Minimum time for laser induced amorphization of Ge<sub>2</sub>Sb<sub>2</sub>Te<sub>5</sub> films”. In: *Journal of Applied Physics* 657.2000 (2016), pp. 657–664.
- [57] Wanhua Yu et al. “Analysis of crystallization behaviour of ge<sub>2</sub>sb<sub>2</sub>te<sub>5</sub> used in optical and electrical memory devices”. In: *Journal of Chemical and Pharmaceutical Research* 6.7 (2014), pp. 415–424.
- [58] Wikipedia. *Silicon elemental info-page*. 2016. URL: <https://en.wikipedia.org/wiki/Silicon> (visited on 07/05/2016).
- [59] Wikipedia. *Gold elemental info-page*. 2016. URL: <https://en.wikipedia.org/wiki/Gold> (visited on 07/05/2016).
- [60] Vladimir P Zhdanov et al. “Plasmonics : Heat transfer between metal nanoparticles and supporting nanolayers”. In: *Physica E* 46 (2012), pp. 113–118.
- [61] Nicolas Large et al. “Plasmonic properties of gold ring-disk nanoresonators : fine shape details matter”. In: *Optical Society of America* 19.6 (2011), pp. 431–437.
- [62] M Rahmani et al. “Influence of plasmon destructive interferences on optical properties of gold planar quadrumers”. In: *Nanotechnology* 22.245204 (2011).
- [63] Janina Fischer et al. “Nanoscale nanocrescent dimers with tunable resonances”. In: *Nanoscale* 3 (2011), pp. 4788–4797.
- [64] Shakeeb Bin Hasan et al. “Nonlinear plasmonic antennas”. In: *Materials Today* 17.10 (2014), pp. 478–485.
- [65] Ekmel Ozbay. “Plasmonics : Merging Photonics and Electronics at Nanoscale Dimensions”. In: *Science* 311.January (2006), pp. 189–193.